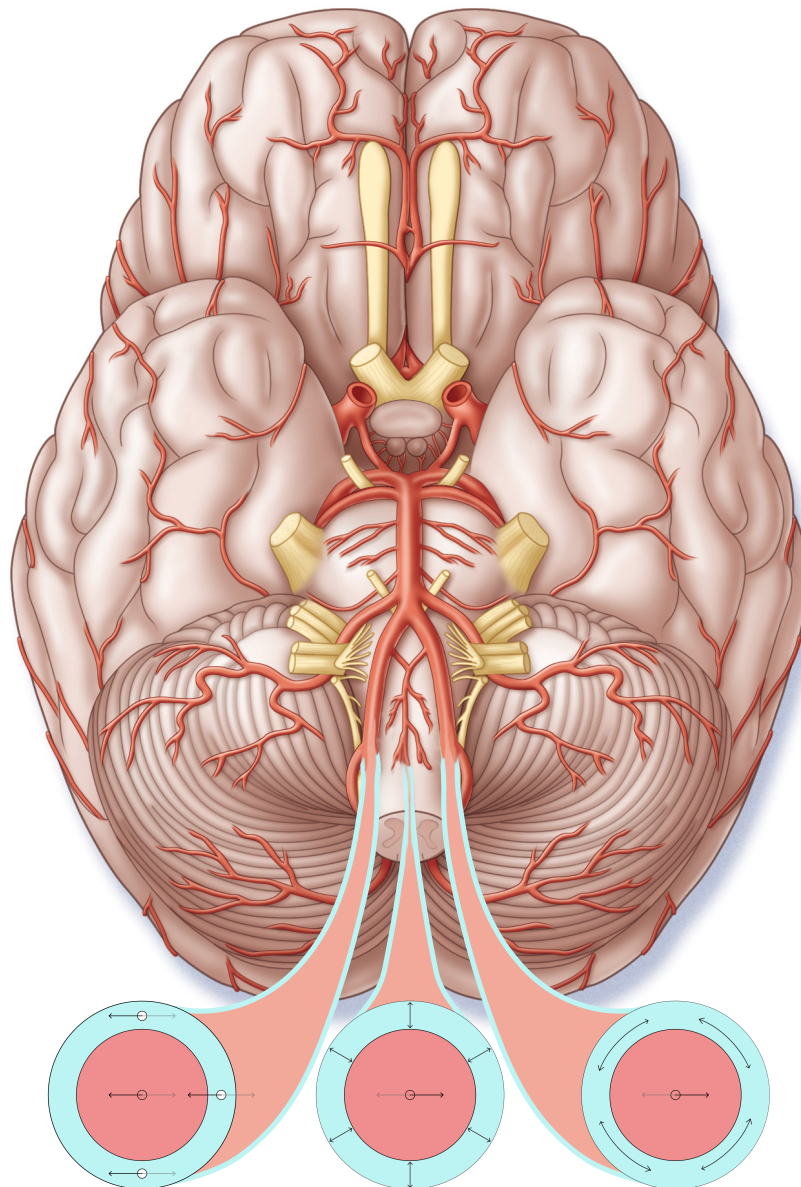


Directionality of CSF-Mobility in the Human Subarachnoid and Perivascular Space



Delft University of Technology - Medical Physics

J.P. Huigen

Directionality of CSF-Mobility in the Human Subarachnoid and Perivascular Space

by

J.P. Huigen

To obtain the degree of Master of Science at the Delft University of
Technology,
to be defended publicly on the 14th of Juli, 2023, at 14:00

Student Number:	4560329
Project duration:	September 1, 2022 - Juli 14, 2023
Thesis Committee:	Thomas Höllt, TU Delft, Supervisor Lydiane Hirschler, LUMC, Daily Supervisor Jaco Zwanenburg, UMCU

This thesis is confidential and is not to be made public until February 14, 2024



Abstract

For several years, the dynamics of cerebrospinal fluid (CSF) in the subarachnoid and perivascular space (SAS and PVS) have been a topic of controversy. Both the SAS and PVS are part of the glymphatic system, a network of CSF-filled regions crucial to waste disposal in the brain. The CSF in this system transports the waste, which is why fluid dynamics are a point of interest when trying to promote brain clearance and keep neurodegeneration at bay. The reason why CSF-dynamics remain unclear, originates in the difficulty to image and visualize them with adequate blood suppression and resolution to ensure that the motion observed is not coming from slow blood flow. For this purpose, a high resolution, CSF-specific magnetic resonance imaging sequence (CSF-STREAM) has been developed, for which a DTI-like metric called CSF-mobility has been derived to quantify fluid dynamics. CSF-mobility is a metric describing the amount of movement that CSF undergoes within a voxel, as a function of intra-voxel dephasing due to bipolar gradients. The metric is derived from the eigenvalues from the tensor information in each voxel (volumetric / 3D pixel) that describes this dephasing along different axes. The orientation of CSF-mobility can also be retrieved from CSF-STREAM data, but has not been characterized yet in detail. This report analyzes the eigenvector orientations of the CSF-mobility tensor in various CSF-filled spaces that are wrapped around blood vessels: the subarachnoid space (SAS) around the middle cerebral artery (MCA) and PVS around arteries in the basal ganglia and centrum semiovale (CSO). In a first experiment, the assessment of local alignment of the SAS and PVS vector field is described. In a second experiment, the first eigenvector (e_1) orientation of each voxel within the SAS and PVS is compared to the local vessel orientation. Three metrics, describing the orientation of the principal CSF-mobility orientation compared to the vessel orientation, are derived: D_{axial} , D_{radial} and D_{spiral} . For each parameter, variations in orientation over the cardiac cycle are analyzed and compared to a random binned signal in order to assess the influence of cardiac pulsatility on each parameter. Results show a clear preference for axial orientations in the SAS, with significant differences when comparing to a negative control ROI ($p < 0.001$), suggesting a difference in orientation patterns or displacement speeds between ROIs. The PVS ROIs indicate only small variations in orientation values from the negative control, with the basal ganglia ROI showing a significant difference from the negative control ($p < 0.05$), but not the CSO ROI. For all ROIs, the influence of cardiac pulsatility on the three parameters is significant when comparing to the random binned signal ($p < 0.05$). Further research on combinations with scalar field approaches and secondary and tertiary eigenvectors and values are advised to further assess what could cause certain directional patterns and reveal more underlying information about the CSF-mobility tensor. Also, data acquisition with multiple b-values could better characterize any possible variations in displacement speeds in different CSF-filled regions.

Preface

In these pages I describe my work on the directionality of CSF-mobility in the human subarachnoid and perivascular space. For the duration of this project, I have been given the opportunity to learn about neurology and magnetic resonance imaging, both of which are subjects that are as interesting as they are intricate.

This project has not been easy and I have relied heavily on the people around me for advice. For that reason, I would like to thank Lydiane Hirschler, Thomas Höllt, Thijs van Osch and my other colleagues at the Gorter group of the LUMC for helping and tolerating me as much as they have. I would also like to thank my parents and my sister for helping me as well. Your moral support has been very valuable to me, even if at times it might not have seemed that way.

I am happy to conclude that I know have a much better sense for how little I know.

Jos Huigen

Contents

1	Introduction	4
2	Background	7
2.1	The influence of echo time on signal decay	7
2.2	Phase and dephasing	8
3	Related Work	11
4	Dataset description	13
5	Preliminary experiment: Assessing local alignment of the CSF-mobility tensor	15
5.1	Methods	15
5.2	Results	16
5.3	Discussion	18
6	Assessing CSF-mobility orientation with respect to vessel orientation	19
6.1	Methods	20
6.2	Results	26
6.2.1	Qualitative assessment shows occurrence of homogeneous regions within the SAS	26
6.2.2	Qualitative assessment of the PVS shows ambiguous results	27
6.2.3	Quantitative assessment of directional CSF-mobility per ROI	28
6.2.4	Comparison between cardiac and random binned signal	29
6.3	Discussion	34
6.3.1	Directional CSF-mobility differences between ROIs	34
6.3.2	Relating the motion-sensitizing gradient strength sensitivity to directional CSF-mobility	35
6.3.3	Reliability of D_{axial} , D_{radial} and D_{spiral}	35
6.3.4	Differences in qualitative and quantitative assessment	35
6.3.5	Amplitude of CSF-mobility orientation change with cardiac and random cycle across ROIs	36
6.3.6	Limitations	37
7	Conclusion	38

Chapter 1

Introduction

The brain is the most energy-consuming organ of the human body [1]. When a cell consumes energy, waste is produced that needs to be disposed of. In the rest of the body, the disposal of waste products is regulated by the lymph vessel network, which takes up waste and transports it to the kidneys [2]. However, the brain does not contain any lymph vessels, which begs the question: If the metabolic rate of the brain is so high, how does it dispose of its waste?

The cerebral vasculature has some features that differ from the vasculature of the rest of the body. One feature that teaches us about waste disposal in the brain is the perivascular space (PVS). As the name suggest, this is a space that surrounds the vasculature, with its inner wall being the blood vessel and the outer wall consisting of the astrocytic endfeet that have wrapped themselves around the vessels (see Figure 1.1).

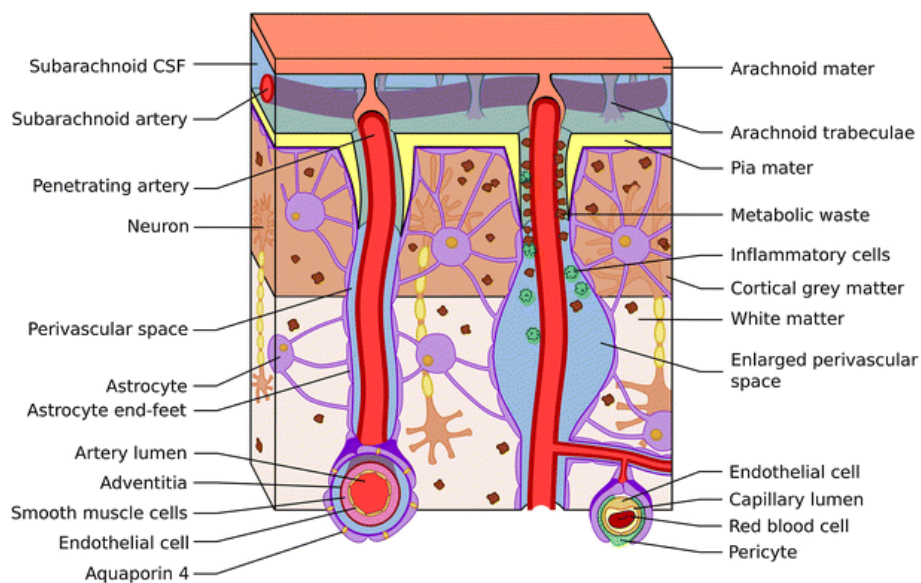


Figure 1.1: The PVS around an artery penetrating the brain parenchyma. Note that two vessels are shown, one with an enlarged PVS, which is often linked to neurodegeneration [3].

PVS are filled with cerebrospinal fluid (CSF), of which recent articles have suggested that it is in constant exchange with the interstitial fluid (ISF) [4]. The interstitium is the space between (brain) cells and is filled with fluids, metabolites and waste products. This knowledge bolsters the thought that the PVS take up the metabolites produced in cells through exchange with the ISF and might in fact be the lymphatic system of the brain. In 2012, Iliff et al. has called this the glymphatic system. The astrocytic endfeet that comprise the outer wall of the PVS are part of glia cells, hence the name [5].

Impaired functioning of the glymphatic system has been linked to a number of neurodegenerative diseases and thus a better understanding of this system might result in helpful tools for prevention or treatment of such diseases. This brings us to question the dynamics of CSF inside the PVS: How do

solutes get transported through these channels? On this question, there are three schools of thought: The glymphatic model [5], the intramural periaxonal drainage (IPAD) pathway [6] and the mixing model [7, 8]. These theories disagree on a multitude of subjects such as the location of the pathway, direction of the CSF-motion, the differences between flow and diffusion and how those concepts contribute to the transport of waste (see Figure 1.2). Furthermore, the IPAD model proposes that vasomotion is the main driving force for solute transport, while cardiac pulsatility is thought to be the main driving force for the glymphatic model [9].

The transport of molecules is an essential link in many physiological and pathological processes of the brain. Since neurodegeneration has been linked to such transport processes in the PVS, several papers have been written on flow and diffusion in the PVS [10, 11]. For most experimental studies, invasive techniques were applied and often conclusions were drawn in humans based on animal models. For instance, Mestre et al. have injected mice with fluorescent microspheres and tracked their displacement via two-photon microscopy [12] and Iliff et al. have used contrast enhanced MRI to visualize the perivascular pathway in rat models [13]. However, using a tracer can alter the dynamics of the medium that it is injected in. As such, findings from tracer-research might not be as insightful for the real dynamics of the PVS as one would hope. Secondly, it is always preferred to confirm findings in animal models with similar findings in humans. Because of this, non-invasive MRI is used to research PVS in humans as well (see also Section 3), but there is a challenge in doing so: Since the PVS is surrounding the blood vessel, a high spatial resolution is needed to disentangle signals from both compartments. Also, to be sure that the measured signal pertains to CSF from the PVS and not slow blood flow, an ultra-long echo time (TE) is warranted to make sure that the blood signal has fully decayed and that the signal we measure is from CSF only. However, phase-contrast MRI, which is the standard for flow analysis in blood vessels, is unfeasible due to its increased susceptibility to artefacts when using a long TE. Therefore, analysis of the PVS with an ultra-long TE is done using a technique similar to diffusion tensor imaging (DTI) [14].

For this purpose, a non-invasive, high-resolution (0.45 mm isotropic) and CSF-specific MRI sequence has been developed by Hirschler et al. to characterize CSF-mobility throughout the entire human brain [15]. This sequence is called the CSF-STREAM sequence. CSF-mobility is a DTI-like parameter that is sensitive to slow flow or back-and-forth motion (more details in Section 2.2 and 3). This was achieved with an accelerated 7 Tesla MRI, by exploiting the magnetic properties of CSF (T₂-preparation and an ultra long TE) and introducing motion sensitizing gradients to probe CSF-mobility along various axes. In this sequence, the bulk of signal within each voxel is attributed to the presence of CSF. The more CSF is within a voxel, the higher the signal-to-noise ratio (SNR), which is directly related to the reliability of the principal direction of diffusion e_1 [16]. In the study by Hirschler et al. that analyses CSF-mobility within the PVS, it has been shown that the sequence can provide a pulsatile CSF-mobility signal that indicates that the sequence can detect physiological effects in PVS. These findings were compared to findings on CSF in the subarachnoid space (SAS) in order to differentiate between both anatomies.

So far, there has not been any research on the directionality of CSF-mobility in the PVS, nor in the SAS. As such, the goal of this study is twofold: (1) To assess the directionality of CSF-mobility within the PVS and SAS and (2) to provide a physiological basis of such parameters by studying the influence of cardiac pulsatility, one of the driving forces for CSF-mediated brain clearance.

The main findings of the report describe a method for the comparison of the CSF-mobility vectors within the PVS and SAS to a centerline fitted through vessels that are surrounded by said SAS or PVS. This method provides insight into the patterns behind fluid dynamics of CSF-filled spaces and clear differences are reported between the SAS and PVS. The parameters that were derived to describe CSF-mobility with respect to vessel orientation all demonstrate a clear pulsatile pattern that is significantly influenced by cardiac pulsatility, which contributes to other findings in literature.

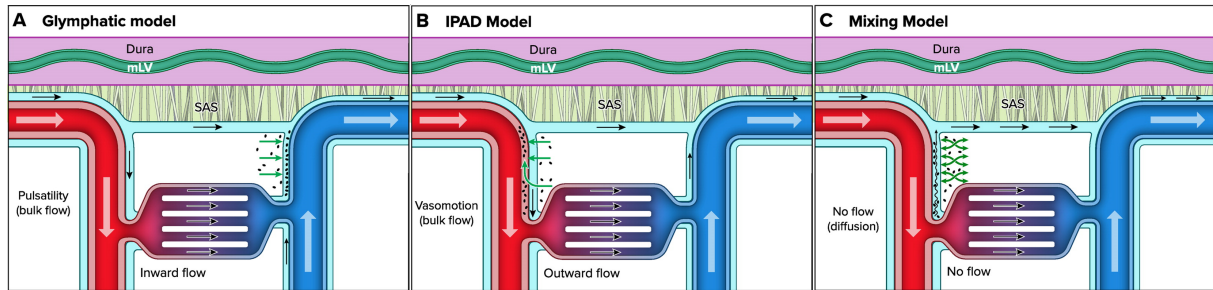


Figure 1.2: Different theories for cerebral waste pathways. The brain parenchyma is depicted as white. **A:** The glymphatic model, which assumes flow in the subarachnoid space (SAS) as well as in the PVS around the vasculature penetrating the parenchyma. Flow in the PVS is assumed to follow the same direction as the blood (arterial inflow, venous outflow). **B:** The IPAD assumes that waste is disposed of through a different channel than the PVS, namely inside the vessel wall (the intramural passage). **C:** The mixing model assumes flow in the SAS, but no flow in the PVS at parenchyma level. Diffusion is seen as the main driving force for solute movement there and thus inflow and outflow of solutes can occur within the same channel [8].

Chapter 2

Background

This chapter provides an explanation to the fundamentals behind the MRI sequence that is employed in this study, which are only a small part of the fundamentals of MRI as a whole. Specifically, the influence of echo time on the acquired signal and the concept of dephasing and its various causes will be elucidated.

2.1 The influence of echo time on signal decay

In MRI, the signal that is measured is excited by applying radio-frequency pulses to proton spins. After applying the RF pulse, a signal that was originally oriented in the longitudinal plane of the magnetic field, is flipped to the transversal plane. There is only a limited time that one can detect the transverse signal before it decays (relaxes) to negligible amounts. Each tissue or fluid has its own decay time constants, called $T1$ and $T2$. The $T1$ constant describes the time it takes for longitudinal part of the signal to recover to $100 * (1 - e^{-1}) \approx 63\%$ of its original signal. The $T2$ constant describes the time it takes for the transverse part of the signal of a certain tissue or fluid to reduce to approximately 37% of its original signal strength. The relation between the measured signal, called M_{\perp} and this decay time is given as follows:

$$M_{\perp}(t) = M_{\perp}(t=0)e^{-t/T2} \quad (2.1)$$

When attempting to discern different tissues or fluids, discrepancies in $T1$ and $T2$ can be exploited. For this study, $T2$ -weighting is applied to maximize signal differences in tissues based on their $T2$ times. Appropriately deciding when to measure the signal (this point in time is called the echo time, or TE) can make it so that differences in signal between different tissues or fluids, and thus the image contrast, are maximized [17].

In our case, the goal is slightly different, since we do not necessarily try to maximize the differences between CSF and blood. The aim of our sequence is to null the blood and tissue signal in order to make sure that the signal we measure solely originates from CSF. $T2$ times for arterial blood and CSF are 68 ms and 1 s, respectively, at 7 Tesla [18, 19]. When modelling the decay of the signal over time, using these decay constants, we can see how both signals differ from one another (Figure 2.1). For the CSF-STREAM sequence that has been applied in the study by Hirschler et al. [15], a TE of 495 ms was applied. For both blood and CSF, signal magnitude at this time can be calculated by the following equations:

$$M_{\perp,blood}(TE) = M_{\perp,blood}(t=0)e^{-TE/T2_{blood}} \quad (2.2)$$

$$M_{\perp,CSF}(TE) = M_{\perp,CSF}(t=0)e^{-TE/T2_{CSF}} \quad (2.3)$$

As seen in Figure 2.1, at this point in time the blood signal has been nulled, whereas approximately 63% of the CSF signal is still available.

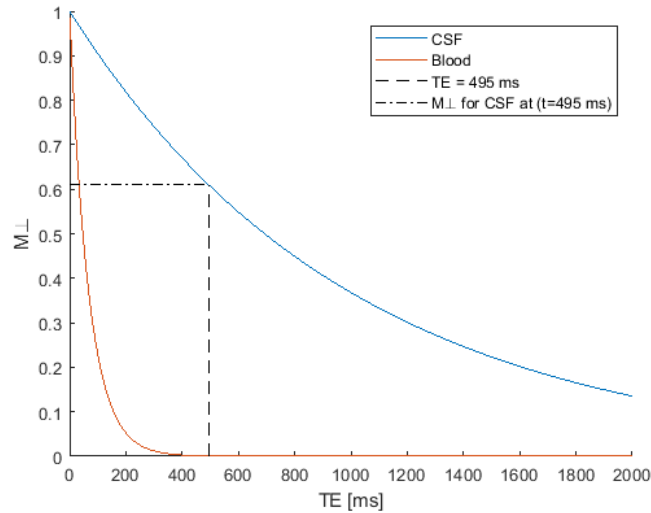


Figure 2.1: M_{\perp} decay for blood and CSF over varying TE. The dotted line represents the time TE=495 ms and the subsequent amount of signal CSF still present.

2.2 Phase and dephasing

In order to understand diffusion weighting in MRI, the concepts of phase and dephasing of proton spins need to be elucidated. When a magnetic field gradient is applied, the amount of magnetic field strength that a spin is subjected to is dependent on the position of the spin compared to the gradient axis.

Consider the following Figure 2.2:

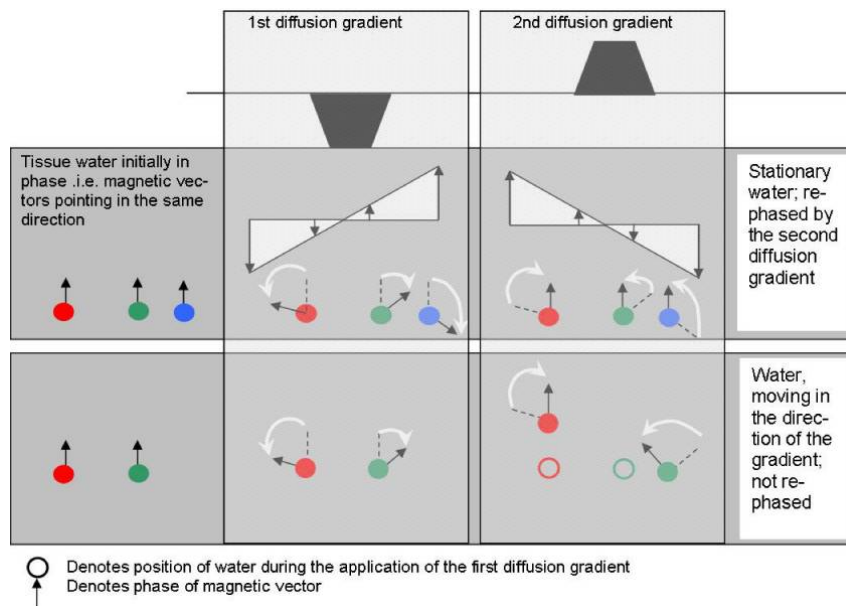


Figure 2.2: Differences in phase for stationary and moving water [20].

In this figure, a positive and negative magnetic gradient following each other is illustrated. This is called a bipolar gradient. Two different groups of spins are represented: One group of static spins (top row) and a group of moving spins (bottom row). When spins remain static, the phase accumulated during the positive gradient lobe is fully refocused by the second, negative gradient lobe. This altogether leads to no phase accumulation by static spins at the end of the application of the gradients. In the bottom row, the red spin is moving upwards, while the green spin moves to the right. The

gradient axis spans from left to right, so in terms of subjected field strength, the red spin experiences no difference between the positive and negative lobe. On the contrary, for the green spin, it is seen that the amount of phase accumulated during the first lobe is not the exact opposite of the amount of phase from the second lobe. When talking about phase, one can recognize the amount of phase that a single spin has accumulated, but also the total phase of multiple spins. In the static spin case, both are the same, since all spins are oriented the same after the bipolar gradient. In the moving spin case, both spins have accumulated a different amount of phase. This causes a discrepancy between the phase of both individual spins. Adding the vectors of both spins together will result in a vector with a magnitude that is smaller than a vector that is the result of adding two vectors with the same orientation. This specific cause for loss in magnitude is called dephasing. [17, 20]

Now consider the next figure, Figure 2.3:

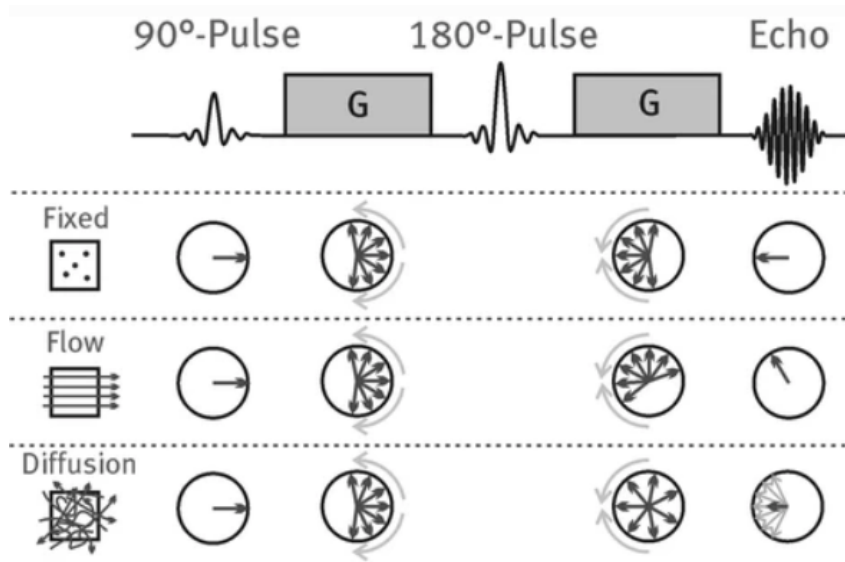


Figure 2.3: Different behavior of spins under the influence of a bipolar gradient. In this case, both gradients have the same polarity, but spins are flipped by the 180°-pulse, which has the same result [21].

In this figure, three different situations with multiple spins are shown. The top row contains stationary spins, the middle row contains spins that flow along the gradient axis coherently and the bottom row contains spins that move incoherently through space. Note that in this figure, both gradient lobes are positive, but there is a 180 degree pulse in between. This has essentially the same effect as the gradient lobes in the first image, which is why the second lobe can also be seen as the "negative" lobe of the two. During the positive lobe, a similar phenomenon occurs for all three situations: Each spin accumulates phase based on their position compared to the gradient axis, which causes them to dephase from one another. At this point, the net vector of all spins in all situations will be equally small. During the second lobe, the phase of the static spins will get refocused again. This causes the resulting net vector to have no phase and the same magnitude as before; after the whole sequence, there is no remnant phase and no dephasing (in the image, the phase is 180 degrees, but this is because of the 180 pulse in between both lobes). In the plug flow case, the spins do not get refocused and accumulate the same phase, which is proportional to their velocity/displacement. This results in all the vectors pointing in the same direction, so the magnitude of the net vector is of the same magnitude as before the sequence, but the net vector direction is different. This means that, for this group of spins, there is phase accrual, but no dephasing. For the bottom row, representing spins in diffusion, there is not only a difference in net phase between before and after the bipolar gradient, but also a difference in the net phase between each spin. This provides both phase and dephasing.

In MRI, the net phase of a signal is proportional to the speed of displacement of a medium, while dephasing, or signal attenuation, is used to determine the incoherence of motion. Note that incoherent motion can occur in different forms, which is illustrated further by Figure 2.4.

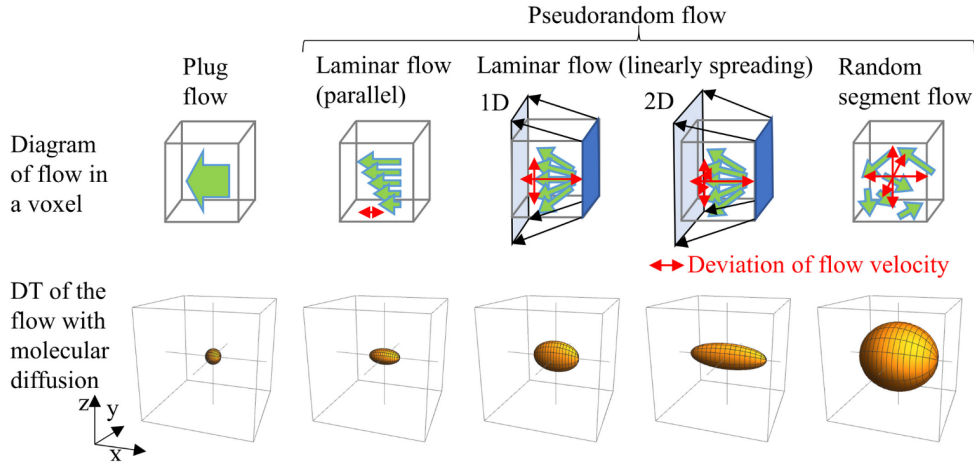


Figure 2.4: Ellipsoids representing various diffusion tensors (DT) under the influence of different fluid dynamics [22].

Figure 2.4 displays different flow profiles and their subsequent diffusion profiles, illustrated as 3D ellipsoid. In the leftmost image, coherent flow or plug flow is shown, which constitutes no variations in the diffusion profile as there is no axis along which there is more dephasing than another. However, when looking at the laminar flow profile and the pseudorandom flow profiles, it is illustrated how dephasing influences the diffusion profile, elongating the ellipsoid along the axes where dephasing is most prevalent. However, apart from flow profiles, another example of incoherent motion is diffusion, which is why dephasing is used as a discriminating parameter for diffusion weighted scans. For each scan, one can determine the diffusion weighting and the displacement speeds it is sensitive for. The parameters for these concepts are the b-value and the velocity encoding, or V_{enc} . The b-value determines for what kind of incoherence the scan is sensitive to; for low b-values, the scan is more sensitive for incoherent flow, while for high b-values, the scan is more sensitive to diffusion. For the V_{enc} , a high V_{enc} is sensitive to high displacement speeds and a low V_{enc} is sensitive to low displacement speeds [22, 23]. Relating all this to the SAS and PVS, the CSF-STREAM sequence also has a certain b-value and V_{enc} . These have been chosen in such a way that there is signal attenuation visible in both the SAS and PVS so that it is certain that signal with a physiological origin is measured. As a consequence, the b-value is set at 13 s/mm^2 , which makes the sequence sensitive to dephasing from both incoherent flow and diffusion (for reference, diffusion weighted scans usually have a b-value of $> 800 \text{ s/mm}^2$). The V_{enc} is set at 5 mm/s which makes it so that the phase accumulation that, in turn, causes this dephasing is highest around those speeds. Because the signal attenuation in the sequence is a result from both diffusion and incoherent flow, the metric for the amount of dephasing in this (CSF-specific) sequence is called CSF-mobility, meaning an intermediate between both phenomena [24].

Chapter 3

Related Work

The glymphatic hypothesis poses that perivascular fluid movement is driven by bulk flow, while more recent papers have proposed that fast dispersion of CSF tracers in the PVS can be accounted for by mechanical pulsations (i.e. mixing) and thus does not require bulk flow [4, 7]. However, fluid movement in the PVS is yet to be described, because no current technique can measure CSF flow in the PVS.

In a study by Wen et al. on human participants, a diffusion-weighted imaging (DWI) scan with $b = 150 \text{ s/mm}^2$ was applied [25]. This method can not assess flow, but provides insight into the fluid dynamics CSF by acquiring information on the dephasing of CSF signal during different MPGs in three perpendicular directions (x,y and z). Assessment of the signal along the cardiac cycle was done for grey matter (GM), white matter (WM) and CSF that surrounds pial arteries. They report a clear pulsatility in rythm with the cardiac cycle in the CSF-voxel, while seeing no pulsatility in the WM or GM. It should be noted that no suppression of the blood signal was done, so measured signal could have some contribution of (pulsatile) blood signal. Lastly. they mention a lack of resolution for assessing penetrating arteries as these are usually around 0.5-1 mm thick.

Bito et al. conducted another non-invasive diffusion-weighted study on human participants [22]. In this study, both a high (1000 s/mm^2) and a low (100 s/mm^2) b-value were applied in order to assess the contribution of diffusion and slow flow to the received signal. From the maps created using the low b-value (DT_L) and the high b-value (DT_H), they computed mean diffusivity (MD) and fractional anisotropy (FA) for both b-values. Six different ROI's were recognized for assessment, one of which with a low MD and FA, used as control, and five with a high MD and FA, of which one was the SAS around the MCA. Comparison of the (DT_L) and (DT_H) indicate a higher MD value for (DT_L) in some ROI's including the SAS around the MCA. Although they do not interpret that finding in the discussion, it hints at a higher contribution of slow flow in that region. The differences in MD and FA for (DT_L) and (DT_H) can be seen in Figure 3.1. However, like the paper from Wen et al., the influence of blood signal on the measurements has to be taken into account and is also mentioned as one of the main limitations. They report that influence of blood signal could contribute to the higher MD and FA around the MCA.

The technique that is used in this study is based on a sequence that was first proposed by Harrison et al. [14]. This sequence can effectively null blood signal by applying an ultra long TE, of which the details are also described in Chapter 2. In the study by Harisson te al., an intermediate b-value-technique (with $b = 107 \text{ s/mm}^2$) was applied to a rat brain in order to assess CSF-mobility. They reported the most severe attenuation in signal in the SAS around the MCA when applying a motion sensitising gradient which was aligned with the vessel direction, indicating a preference for axial orientation of CSF-mobility in that space. They also reported a clear increase in CSF-mobility during systole and decrease during diastole, indicating the influence of cardiac pulsations. Harrison et al proposed the first non-invasive technique to measure displacements in the SAS around the MCA without interference of blood signal. [14].

In the aforementioned studies, no PVS around penetrating arteries into the parenchyma have been analyzed and only one study nulls the blood signal. The reason for this is that the resolution required for this has not been reached for this specific technique. In the dataset that is used for this study, a resolution of 0.45 mm isotropic was reached, which is adequate for imaging penetrating arteries. This is possible due to the use of a 7T MRI scanner (Wen et al. and Bito et al. used 3T, Harrison et al. used a 9.4T animal scanner) and the use of a turbo spin echo (TSE) readout as opposed to the faster single shot echo-planar imaging (ssEPI) readout. Because the TSE readout takes more time, compressed

sensing is applied to speed up the acquisition process and minimize motion artefacts due to participant discomfort. A b-value of 13 s/mm^2 was applied, as this setting showed signal attenuation in both the SAS and the PVS. Combining the improvements in resolution with the blood nulling from the ultra long TE can thus measure CSF-signal in the penetrating PVS more accurately [24]. Furthermore, directionality of the CSF-mobility tensor has only been assessed using scalar values like MD and FA; no three-dimensional assessment comparing the signal to the vessel orientation has been done.

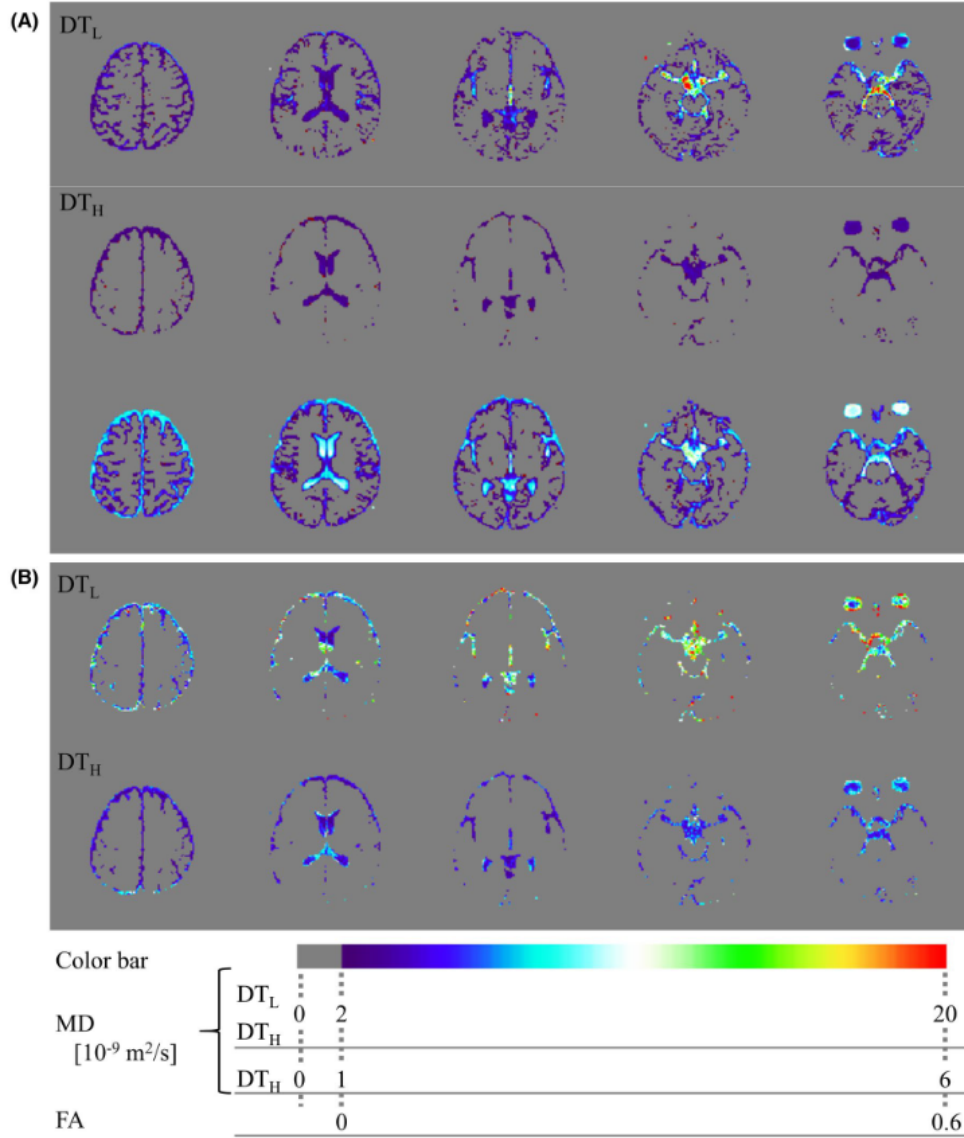


Figure 3.1: Multislice images of MD (A) and FA (B) in the brain. MD of DT_L is visualized using two colorbars. $0 - 20 \cdot 10^{-9} \text{ m}^2/\text{s}$ is used for the upper row and $0 - 6 \cdot 10^{-9} \text{ m}^2/\text{s}$ is used for the lower row, as described in the bottom portion of the figure. When comparing the highest and the second-highest row, the sensitivity to slow-flow rather than diffusion for the MCA region is illustrated [22].

Chapter 4

Dataset description

This retrospective study was conducted on CSF-STREAM (CSF-Selective T2-prepared Readout with Acceleration and Mobility-encoding) data of 11 healthy participants (age: 35 ± 14 years, 8 females, 3 males). One CSF-STREAM dataset consists in seven scans: one non-motion sensitized scan and 6 motion-sensitized scans. The readout was a turbo-spin-echo (TSE)-readout with an echo-time (TE) of 495 ms for the CSF isolation. With this sequence, a resolution of 0.45 mm isotropic was reached. For each participant, the cardiac rhythm was monitored with a finger clip during data acquisition so that each part of the acquired signal could be assigned to one of six cardiac phases. Every dataset per participant was reconstructed twice: Once with retrospective binning towards the cardiac cycle and a second time to random cycles as a negative control. This resulted in six cardiac bins (as there are six cardiac phases) and six random bins. Note that both six-phase datasets are thus derived from the same data. Having derived the amount of signal attenuation along the axes of each of the MPGs, one can construct a tensor containing the CSF-mobility along six equidistant axes. Analysis of the tensor data was done using the first eigenvector e_1 and the first eigenvalue λ_1 derived from the tensor, which was calculated from the values corresponding to the six MPGs. The first eigenvector of each tensor provides the main orientation of the tensor, i.e. the most dominant CSF-mobility direction, while the eigenvalue provides information on the magnitude of CSF-mobility in that direction. For both the preliminary analysis in Chapter 5 as well as the CSF-mobility directional analysis in Chapter 6, the vectors (called $\vec{V}(i, j, k)$, in image processing, indices (i, j, k) are typically used for describing the xyz-coordinates of a voxel) that are analyzed are computed as follows:

$$\vec{V}(i, j, k) = \lambda_1(i, j, k) \cdot e_1(i, j, k) \quad (4.1)$$

For Chapter 5 and 6, three different ROIs are assessed. A slice of the b0-image of the three ROIs used Chapter 5 are shown in Figure 4.1. The largest ROI is on the left: the SAS around the MCA. The other two ROIs are the PVS around arteries in the basal ganglia (middle) and in the centrum semiovale (CSO). As will also be explained in the respective chapter, all the datapoints within the ROI will be analyzed.

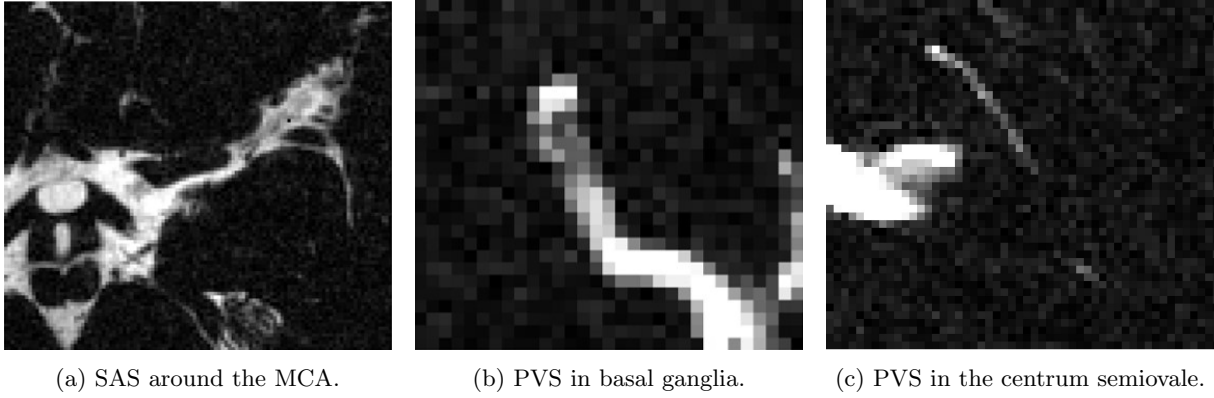


Figure 4.1: Example locations of the ROIs in representative individuals.

For the experiment in Chapter 6, the same ROIs will be used, but one more ROI is added. This last ROI is a slab of dark brain tissue, which is meant as a control to assess fluid dynamics in regions with low CSF and no clear vessel orientation. The description of this fourth ROI and the motivation for its addition is given in the respective chapter.

Chapter 5

Preliminary experiment: Assessing local alignment of the CSF-mobility tensor

In this chapter, the first experiment of the thesis is described. There is not yet any understanding of the vector orientations inside the vessels or in the brain tissue, or how these vectors compare to one another. Therefore, the goal of this experiment is to evaluate how well CSF-mobility vectors are aligned to their neighbours and to compare alignment in CSF-filled regions to alignment in brain tissue, where the concentration of CSF is lower. In doing so, one can assess the CSF-mobility vector fields of different sections of the brain to see whether there is any coherence in orientation and to compare between the different ROIs. This provides a first exploration of the dataset that can be used to decide on how to proceed towards more extensive CSF-mobility analysis.

5.1 Methods

The purpose of this first experiment is to analyze each vector $\vec{V}(i, j, k)$ within a three-dimensional space and compare with its neighbours. The aim is to propagate $\vec{V}(i, j, k)$ from the voxel origin in the positive and negative direction in order to find the two neighbouring voxels that $\vec{V}(i, j, k)$ is pointing at. The orientation of the vectors in these neighbouring voxels are then compared to the orientation of the central vector by doing a dot-product.. These can be any 2 opposing voxels in a 3x3x3 space surrounding the central vector. In order to find to which two voxels $\vec{V}(i, j, k)$ is pointing to. The coordinates of those voxels need to be defined in terms of the origin of $\vec{V}(i, j, k)$ and its orientation. For this purpose, three shifting values (a, b, c) which depend on the orientation of the normalized vector $\vec{V}(i, j, k)$, which is $\vec{e}_1(i, j, k)$ are defined: If $e_{1,x}(i, j, k) > \sin(\frac{\pi}{8})$, $a = 1$ and if $e_{1,x}(i, j, k) < \sin(-\frac{\pi}{8})$, $a = -1$. This value of $\frac{\pi}{8}$ is chosen as this is the angle at which the e_1 vector would point exactly at the point where two corners of a voxel meet (see leftmost image in Figure 5.1). If none of these requirements are met, the shifting value is set to zero. The same is done for values b and c by assessing $e_{1,y}(i, j, k)$ and $e_{1,z}(i, j, k)$, respectively. This defines the indices of the neighbouring voxel in the positive vector direction as $(i + a, j + b, k + c)$. For the negative vector direction, the sign is flipped so that the indices are $(i - a, j - b, k - c)$. The orientations of both opposing vectors are compared with the orientation of the central vector to get a scalar value $P(i, j, k)$ that is assigned to the central vectors voxel. A high value $P(i, j, k)$ means that the vector $\vec{V}(i, j, k)$ of the center voxel is highly parallel to its neighbours $\vec{V}(i + a, j + b, k + c)$ and $\vec{V}(i - a, j - b, k - c)$. This value is computed for the original $e_1\lambda_1$ vectors, shown in Equation 5.1, as well as for normalized vectors e_1 , shown in Equation 5.2 (\cdot indicates the dot-product between vectors):

$$P(i, j, k) = |\vec{V}(i, j, k) \cdot \vec{V}(i + a, j + b, k + c)| + |\vec{V}(i, j, k) \cdot \vec{V}(i - a, j - b, k - c)| \quad (5.1)$$

$$P(i, j, k)_{norm} = |\vec{e}_1(i, j, k) \cdot \vec{e}_1(i + a, j + b, k + c)| + |\vec{e}_1(i, j, k) \cdot \vec{e}_1(i - a, j - b, k - c)| \quad (5.2)$$

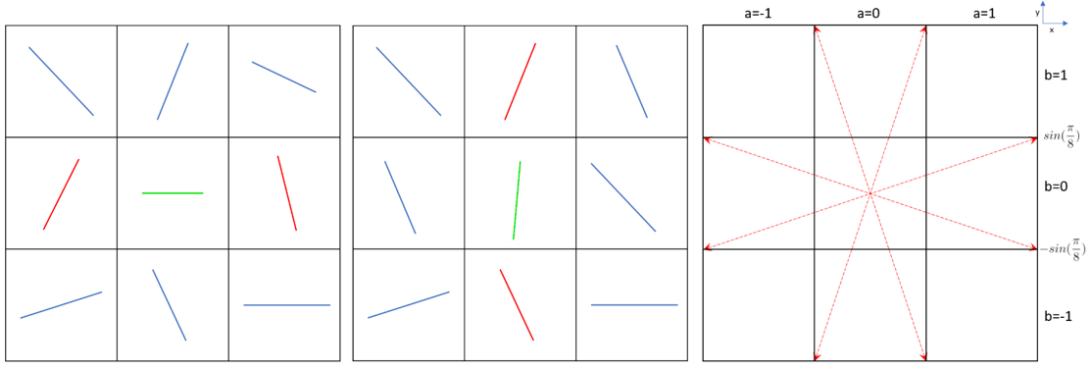


Figure 5.1: Schematic of the preliminary image analysis method in a 2D example. $\vec{V}(i-a, j-b)$ and $\vec{V}(i+a, j+b)$ are highlighted in red and the central voxel to which the value $P(i, j)$ will be assigned is highlighted in green ($P(i, j, k)$ in a 3D example). The left and middle image show the differences in orientation between low (left) and high (middle) local alignment values. The rightmost image indicates the how the orientation of the central vector is related to the shifting values, with an example for $e_{1,y}$, which determines shifting value b .

A schematic overview of how to find $\vec{V}(i+a, j+b, k+c)$ and $\vec{V}(i-a, j-b, k-c)$ in a 2D space can be seen in Figure 5.1. The computation is applied to each vector in a pre-defined three-dimensional space. Voxels on the edge of the space are not computed. A three dimensional scalar field is created with these values and compared to the b0-image of the DTI sequence. If the corresponding vector \vec{e}_1 or $\vec{e}_1\lambda_1$ of some voxel is aligned with neighbouring vectors $\vec{V}(i+a, j+b, k+c)$ and $\vec{V}(i-a, j-b, k-c)$, a relatively high value is assigned to that voxel. When high local alignment values coincide with high CSF-values in the b0-image, the case can be made that there is some degree of homogeneity in the vector field of the CSF around the vessel. Furthermore, under the assumption that the vectors in the CSF-filled vessels have a similar orientation, a certain amount of contrast is expected between the $P(i, j, k)$ values within the PVS or SAS and outside, in regions containing little CSF. The comparison between both methods (local alignment values for the normalized and unnormalized vectors) can provide insight into the occurrence of alignment: Is local alignment of vectors related to the magnitude of the CSF-mobility, or can regions with low λ_1 also exhibit high amounts of alignment? This can be seen in the results, in Section 5.1.

5.2 Results

In order to check the performance of the processing method that has been described, this method has been applied to a simulated 2D vector field. This vector field has some randomly oriented vectors with a magnitude of 0.05 and some vectors with magnitude 1 that have been manually oriented so that they form a line moving diagonally through the image. Halfway through, the vector line rotates 90 degrees in two steps, as can be seen in Figure 5.2. The example illustrates the difference in performance for straight and curved segments. In the curved segment, we can see that any vector following a curve (some PVS or SAS sections might be curved as well) will also be less aligned with its neighbours and thus give a low value for $P(i, j, k)$. Furthermore, we can see that there are some high values placed randomly around the voxels containing large vectors. This is because here, the randomly oriented, smaller vectors have shifting values that select the larger vectors as their neighbours. The magnitude of the large vector in combination with good alignment constitute relatively high values distributed randomly along the line of large vectors.

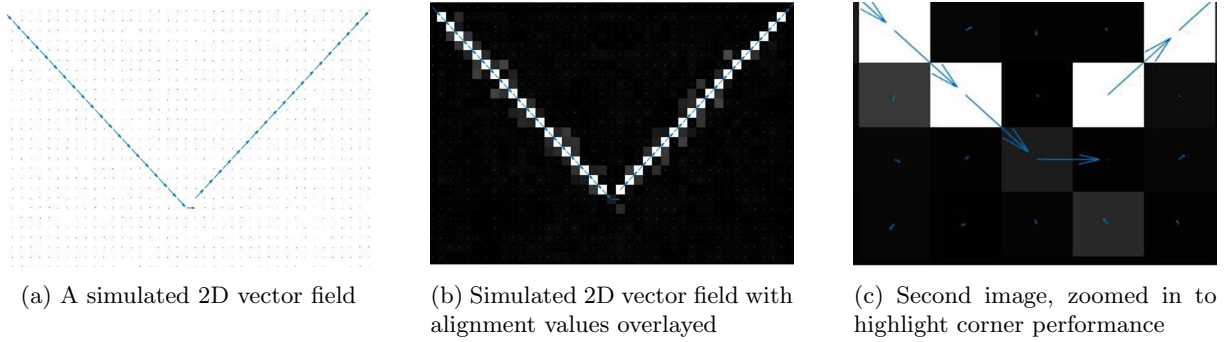


Figure 5.2: The local alignment method from Equation 5.1 performs well on straight segments, but not on corners

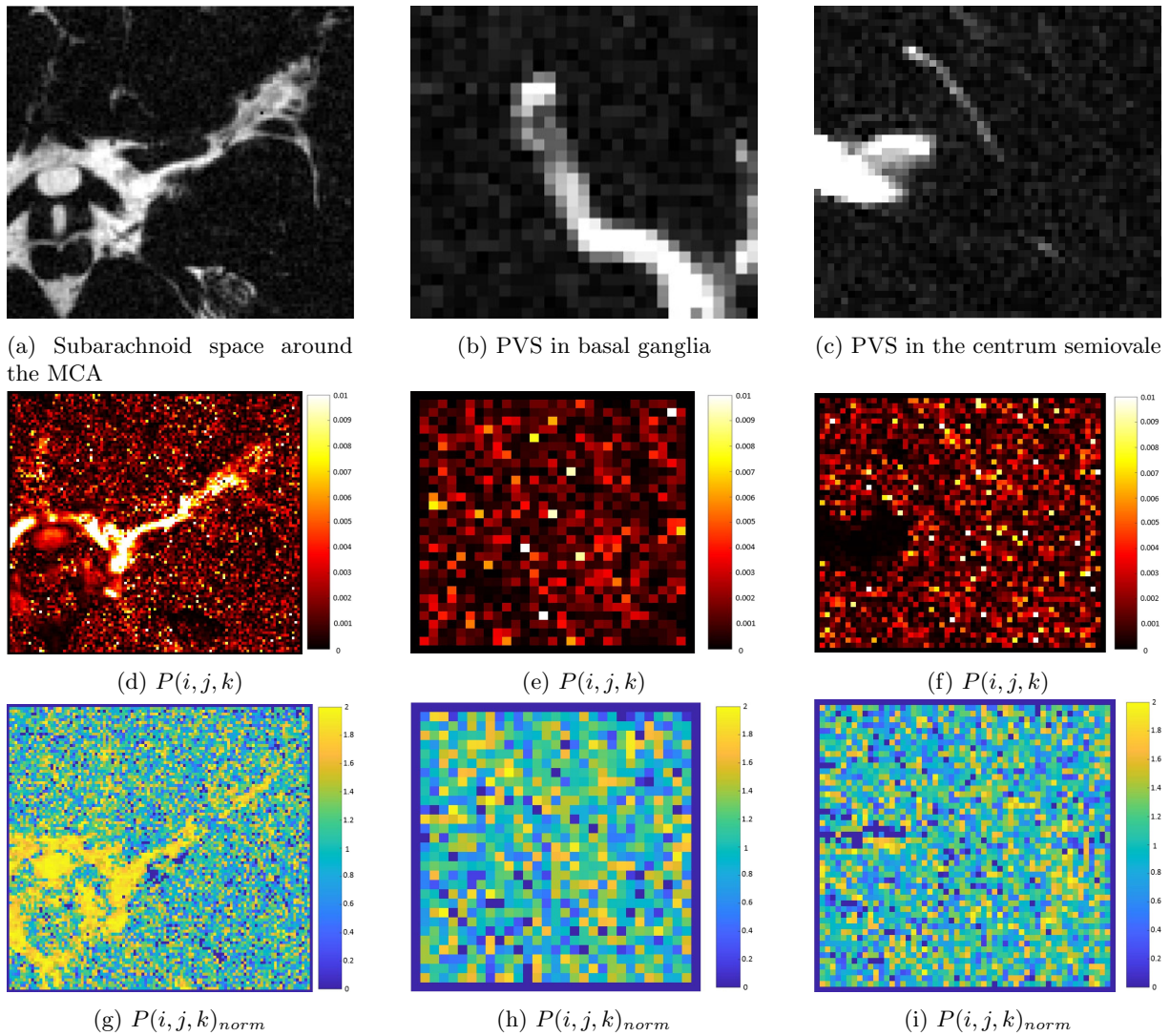


Figure 5.3: The three ROIs and their local alignment images. (a,b,c): Selected ROIs shown on the b_0 -image. (d,e,f): Degree of local alignment of CSF-mobility vectors ($\lambda_1 e_1$). (g,h,i): Degree of local alignment of normalized CSF-mobility vectors ($e - 1$).

Figure 5.3 shows the results of the degree of alignment of CSF-mobility vectors with their neighbors in three ROIs. This analysis has been done for only one participant per ROI. The vector fields that were analyzed originated from the dataset of the first cardiac phase. For all columns, the values in the second row, meaning local alignment of the unnormalized CSF-mobility vector, are highest in the SAS and values in the PVS are rather low compared to this, indicating a difference in either vector length or alignment, or a combination of both. For the third row, we can see that high values are present in all ROIs (by chance, some randomly oriented vectors can be aligned well). When looking at the images from the MCA, vectors in the SAS around the MCA present high values, indicating a high degree of local alignment. The differences between Subfigure 5.3d and 5.3g indicate the influence of e_1 and λ_1 on local alignment values and show that there are some regions that have a high local alignment. Results of the PVS in the basal ganglia and the CSO tell a different story: Both the directionality and the vector magnitude do not constitute sufficient contrast with the CSF-sparse regions. However, a darker part in the middle left of Subfigure 5.3f indicates a significantly lower vector magnitude in this CSF-filled region than its surroundings, since this drop in signal is not seen in Subfigure 5.3i.

5.3 Discussion

The results from the local alignment assessment indicate a high degree of alignment in the SAS, while no alignment is demonstrated in the PVS ROIs. These findings could be explained by more laminar flow profile in the SAS and more turbulence in the PVS. Another explanation could be the influence of noise in these regions, as PVS ROIs are thinner than the SAS. Furthermore, the angle of directional change in the smaller segments could possibly be too steep, performing in a similar way as the example in Figure 5.2. However, that does not explain the low signal in straighter parts of the segmentations. Note that this method is only sensitive to parallel vectors that are in line with each other. Vectors that are parallel, but ordered sideways of one another and not along, do not get assigned high values.

Overall, this method indicates a clear difference in alignment between SAS and PVS, but it is too limited for any profound conclusions on the dynamics of PVS. Going forward, comparing the CSF-mobility vector orientation to the vessel orientation located within the CSF-filled space, instead of comparing CSF-mobility vectors to each other, could provide more insight. This is because the influence of (potentially noisy) neighbouring vectors would then not perturb the assigned values.

Chapter 6

Assessing CSF-mobility orientation with respect to vessel orientation

This chapter describes the main experiment of the thesis: Analyzing the orientation differences of CSF-mobility vectors in the SAS and PVS with respect to the orientation of the vessel located within the CSF-filled spaces. For this purpose, we envision three characteristic directions of CSF-mobility: Axial (along the longitudinal vessel axis, see top of Figure 6.1), radial (moving in an outward from the longitudinal vessel axis, see middle of Figure c6.1) and spiral (swirling or spiraling around the vessel axis, see bottom of Figure 6.1). Figure 6.1 represents a cross-sectional view of the characteristic motion of all three directions in the PVS. The aim of this experiment is to express the e_1 orientation of each voxel in terms of these three characteristic directions. The ROIs that are to be analyzed are the same as in the first experiment, but one more ROI is added. This fourth ROI is a single slice of brain tissue that contains a low concentration of CSF. Specifics on the ROIs and the mathematical definitions of these directions will be given in in Section 6.1.

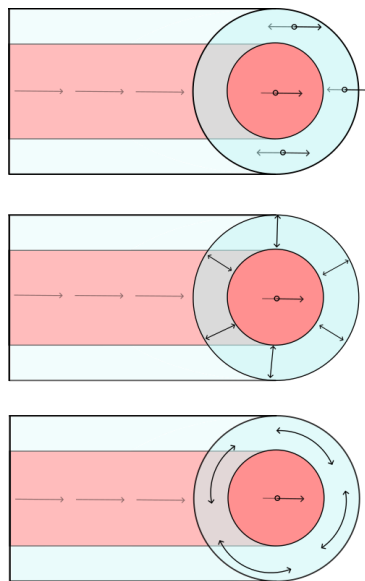


Figure 6.1: From top to bottom: Axial, radial and spiral CSF-mobility in the PVS. The red part signifies blood and the light blue CSF. Note that in smaller vessels such as in the basal ganglia and CSO, the diameter of the blood segment is so small that it is not visible.

The reason for defining these three parameters is to compare the direction e_1 of each CSF-mobility vector to the local vessel orientation. Metrics for axial and spiral CSF-mobility could provide insight into the freedom of movement along the vessel walls, possibly indicating transport of fluids from the larger CSF-filled spaces to smaller PVS. Radial CSF-mobility can be influenced by radial movement in

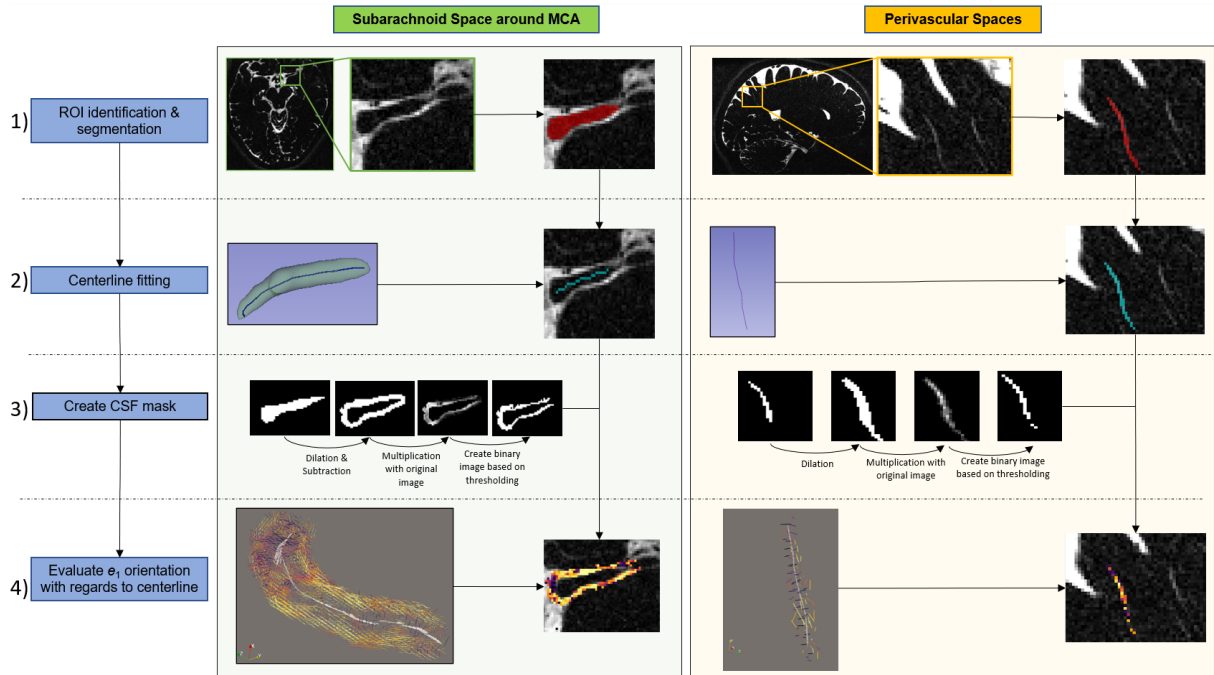


Figure 6.2: Visualization pipeline for analysis of the CSF-mobility vectors. Images from ITK-SNAP (Step 1), 3D Slicer (Step 2), MATLAB (Step 3) and Paraview (Step 4) are incorporated in the figure. Each of the steps is also explained in detail in Section 6.1.

the vessel such as cardiac pulsations or vasomotion, or possibly interaction between the PVS and the parenchyma.

6.1 Methods

The following section describes how the directionality of each \vec{e}_1 is compared to local vessel orientation. The approach for assessment of CSF-mobility vector orientation in SAS and PVS can be divided up into 4 steps:

1. The identification and segmentation of each ROI, based on anatomy. Doing so makes it possible to differentiate between CSF-mobility characteristics of the SAS, the PVS around different vasculature, and regions containing low amounts of CSF.
2. The fitting of a centerline through each vessel. This part is crucial to acquiring information on local vessel orientation.
3. Creating a CSF mask which will identify the voxels containing information that is relevant to the research question and exclude voxels that are not.
4. Directionality assessment of the CSF-mobility vector compared to the vessel orientation.

A visualization of the process can be found in Figure 6.2. In the following sections, each of these steps will be explained in detail.

ROI identification and segmentation

For each participant, the same regions as used in Chapter 5 were selected for further assessment, together with a region of darker brain tissue that did not contain any visible PVS. This darker brain tissue region is intended to be used as a negative control in which there are no anatomical borders visible that might produce an average preferential direction. To perform the ROI identification and segmentation, the b0-image of each participant was loaded into ITK-SNAP (version 3.8.0). For the MCA, the black region of blood within the vessel was selected manually. This is the region that is

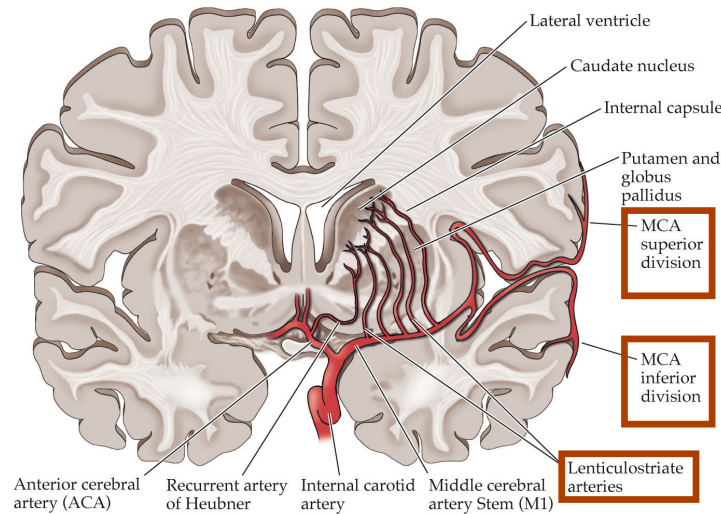
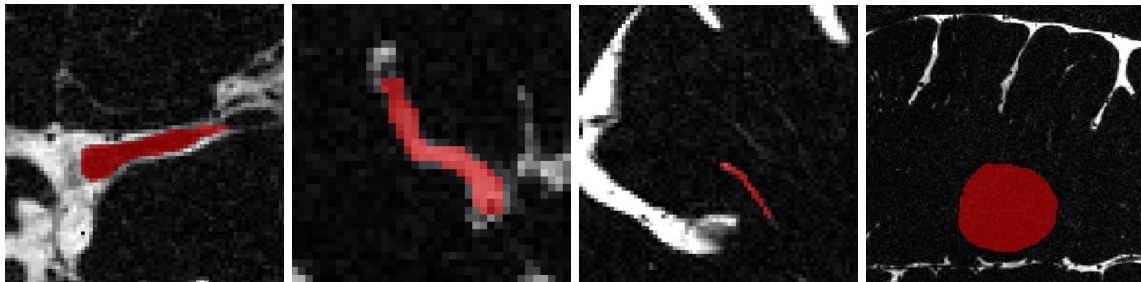


Figure 6.3: Schematic of the MCA [26].

encompassed by the CSF in the SAS. The full segmentation stretched from the point where the internal carotid artery (ICA) branches into the MCA to the point where the MCA bifurcates into its superior and inferior parts (see Figure 6.3). For the PVS in the centrum semi ovale (CSO) and basal ganglia, the CSF signal of the vessel was selected manually through slices for as long as it was visible. Care was taken to choose a long PVS so that the amount of available datapoints would be maximized. Lastly, a brain-tissue ROI (from now denoted as "tissue") containing little CSF (defined as low signal intensity on the b₀-image by a threshold of < 60) was selected within each participant for comparison. The motivation for including such an ROI is to be able to compare ROIs where the vessel geometry implies a clear orientation preference (vasculature around which the SAS and PVS are located) to an ROI with no apparent preference (no visible vasculature). For this ROI, a single slab of voxels (meaning from one axial slice) from a dark region in the b₀-image was chosen. This ROI was selected in the upper middle region of the left hemisphere. Care was taken to make sure every tissue ROI was roughly the same size. Examples of the ROIs in the anatomical context are found in Figure 6.4.



(a) Segmentation of the blood in the MCA (axial) (b) Segmentation of the PVS in the basal ganglia (sagittal) (c) Segmentation of the PVS in the CSO (sagittal) (d) Segmentation of the dark tissue slab (axial)

Figure 6.4: The 4 ROIs within each participant to be analyzed. The highlighted red part is the same as the segmentation from which the CSF-mask is created: In the leftmost image in Figure 6.6, the geometry is the same as the geometry of the MCA in this figure.

Centerline fitting

In order to compare each CSF-mobility vector with the vessel orientation, (for each cross-sectional segment, this is the vector perpendicular to the cross-section plane), a centerline is fitted through each vessel. To achieve this, each segmentation that was made in ITK-SNAP was imported into 3D Slicer (Version 5.2.2), in order to fit a centerline through the segmentation. For this, the "Extract Centerline"

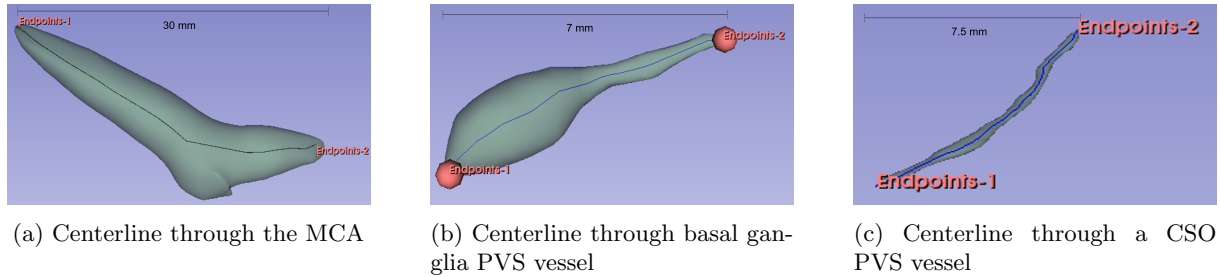


Figure 6.5: The three regions of interest, with a scale for reference. Note that the segmentation for (a) is based on the blood, while the segmentation for (b) and (c) is based on the CSF signal.

tool from the Vascular Modeling Toolkit was used. In figure 6.5, screenshots of the different segmentations with their corresponding centerline can be seen. Note that these pictures are not of the same scale. Each centerline was saved as an OBJ-file. In order to make the saved OBJ-files useable in the MATLAB environment, the coordinates points within the file were scaled to the right resolution and rotated to the right frame of reference. Each of the centerlines was plotted within the b0-image and checked to make sure that the affine transformations were done correctly. Tangents for each centerline coordinate were created by subtracting the current position coordinates from the next position coordinates and saved.

Creating a CSF mask

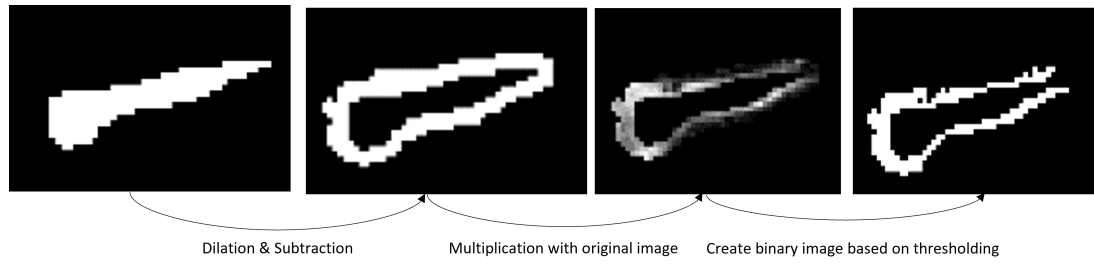
For each ROI, the voxels that are classified as either SAS or PVS surrounding the chosen vessel need to be identified as such. These voxels all need to meet two criteria: The signal in the b0-image needs to be sufficiently high to ensure the ROI contains only CSF-signal and the voxels need to be part of either the SAS or the PVS surrounding the vessel. For the SAS around the MCA, as seen in Figure 6.4, the blood compartment in the vessel is visible, while in the PVS, the vessel diameter is so small that no blood compartment is visible. This fact makes the steps for defining an SAS mask inherently different from the steps for defining a PVS mask. Both masks were created in MATLAB (version 2019b), based on the segmentations from ITK-SNAP. This mask is applied to all CSF-mobility vectors to be analyzed. For the subarachnoid space around the MCA, the segmentation, which is a binary image, was dilated with a spherical element that had a diameter of 11 voxels. Then, the original segmentation was subtracted from the image and the subsequent mask was applied to the b0-image, so that the blood from the MCA is not included in the mask, but the CSF in the SAS surrounding the blood is. This 3D mask was then thresholded so that only voxels above a grey value of 80 were kept. For the PVS, the same steps were taken, but there was no subtraction as the segmentation made in ITK-SNAP was drawn based on CSF-filled regions. Also, the dilation for the PVS was done with a spherical element that had a diameter of 3 voxels. See Figure 6.6 for a graphical explanation.

CSF-mobility vector orientation assessment

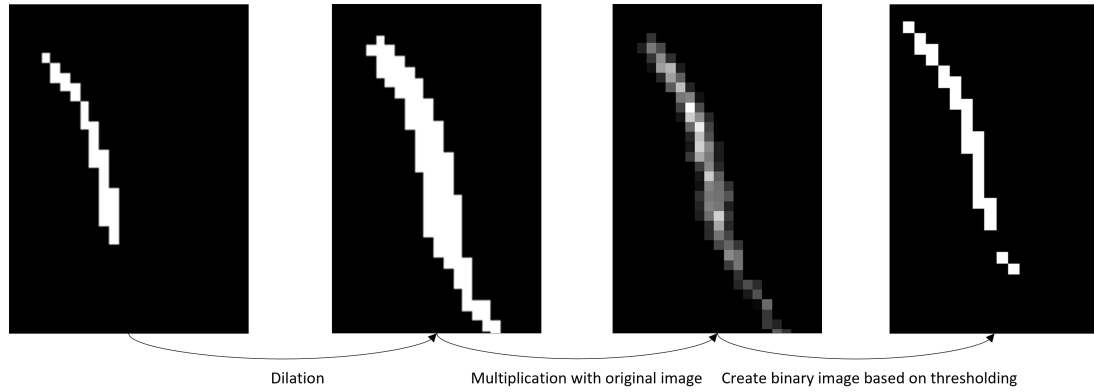
Once the list of coordinates that were included in each ROI was created based on the CSF-mask, each datapoint corresponding to those coordinates was linked to the centerline tangent closest to that point (denoted as \vec{v}_{tang}). For computing the tangent, the following equation was applied:

$$\vec{v}_{tang}(k) = \vec{c}(k+1) - \vec{c}(k) \quad (6.1)$$

Where $\vec{c}(k)$ is the coordinate vector for interpolated point k on the centerline and k is the number that denotes which point on the centerline is being considered, as the centerline consists of discrete points in 3D-space. For each coordinate, the orientation of the CSF-mobility vector (in this section also denoted as $\vec{V}(i, j, k)$) was compared to the orientation of the centerline tangent that it was linked to. Three different parameters were computed: Axial CSF-mobility (D_{axial}), radial CSF-mobility (D_{radial}) and spiral CSF-mobility (D_{spiral}). For all three parameters, explanation with formulas will now follow, but for a more graphical illustration of all the vectors involved, see Figure 6.7. On the left side of the figure, it is shown how $\vec{V}(i, j, k)$ is decomposed into \vec{v}_{axial} , \vec{v}_{radial} and \vec{v}_{spiral} . Note that each of these three vectors is perpendicular to one another and try to compare their orientation to the more intuitive image



(a) Image processing steps for the SAS around the MCA



(b) Image processing steps for the perivascular space

Figure 6.6: How the CSF-mask was created

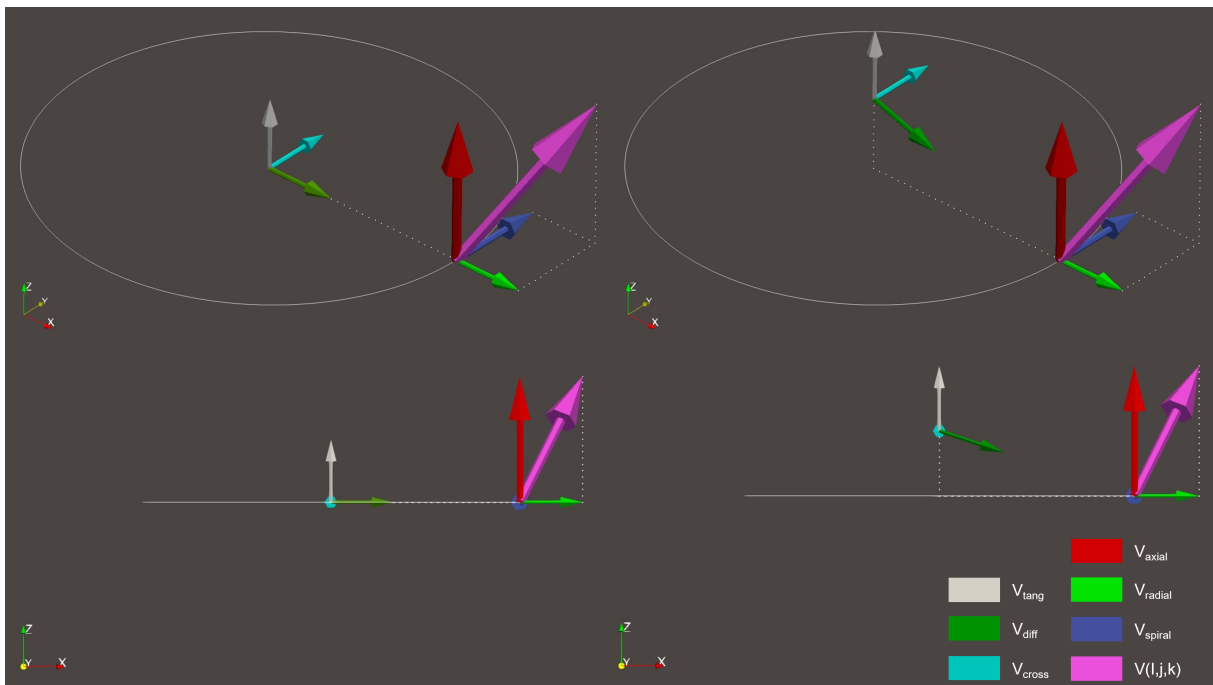


Figure 6.7: Schematic drawing of an example vector $\vec{V}(i, j, k)$ on (left) or beneath (right) a plane perpendicular to \vec{v}_{tang} . Note the difference in orientation between \vec{v}_{diff} and \vec{v}_{radial} in the example on the right.

of the three directions of CSF-mobility shown at the beginning of this chapter in Figure 6.1. For convenience, a coordinate system has been chosen for which the following equations hold:

$$\vec{v}_{axial} = \vec{V}(i, j, k) * \hat{z} \quad (6.2)$$

$$\vec{v}_{radial} = \vec{V}(i, j, k) * \hat{x} \quad (6.3)$$

$$\vec{v}_{spiral} = \vec{V}(i, j, k) * \hat{y} \quad (6.4)$$

Where $*$ denotes element-wise multiplication of both vectors. \hat{x} , \hat{y} and \hat{z} are unit vectors with magnitude 1 pointing in line with the axis they are named after.

The first parameter, Axial CSF-mobility, is defined as a measure for how parallel $\vec{V}(i, j, k)$ is to the closest centerline tangent and can be computed by using Equation 6.5.

$$D_{axial} = \left| \frac{\vec{V}(i, j, k)}{\|\vec{V}(i, j, k)\|} \cdot \frac{\vec{v}_{tang}}{\|\vec{v}_{tang}\|} \right| \quad (6.5)$$

In this equation, \vec{v}_{tang} has already been defined and $\vec{V}(i, j, k)$ is the CSF-mobility vector equal to $\lambda_1 e_1$. Normalizing both vectors by dividing them by their own magnitude produces two vectors that both have a magnitude of 1. Doing the dot-product between both vectors then gives us a measure, ranging from 0 to 1, for how parallel the measured CSF-vector is to the closest point on the tangent line.

The second parameter, radial CSF-mobility is defined as how parallel the orientation of e_1 is to the surface normal of the closest point on the vessel wall, assuming the vessel is a perfect cylinder with orientation \vec{v}_{tang} . In order to understand the Equation that is used to derive this parameter, we first need to define two other vectors. The first is the difference vector \vec{v}_{diff} (which is normalized) between the position of the tangent line (denoted as \vec{v}_t) and the position of vector $\vec{V}(i, j, k)$ (denoted as \vec{v}_m):

$$\vec{v}_{diff} = \frac{\vec{v}_m - \vec{v}_t}{\|\vec{v}_m - \vec{v}_t\|} \quad (6.6)$$

Using this difference vector, one can define \vec{v}_{cross} :

$$\vec{v}_{cross} = \frac{\vec{v}_{tang} \times \vec{v}_{diff}}{\|\vec{v}_{tang} \times \vec{v}_{diff}\|} \quad (6.7)$$

Figure 6.7 visualizes how \vec{v}_{diff} points in the same direction as \vec{v}_{radial} and how \vec{v}_{cross} points in the same direction as \vec{v}_{spiral} . In order to compute radial CSF-mobility measure D_{radial} , we can now apply the Equation 6.8:

$$D_{radial} = \left| \frac{\vec{V}(i, j, k)}{\|\vec{V}(i, j, k)\|} \cdot \frac{\vec{v}_{cross} \times \vec{v}_{tang}}{\|\vec{v}_{cross} \times \vec{v}_{tang}\|} \right| \quad (6.8)$$

In this equation, we do not use \vec{v}_{diff} , but the cross product between \vec{v}_{tang} and \vec{v}_{cross} . The reason for this will be explained in the next section, but for now it should be clear that, for the example on the left hand side of Figure 6.7, this notation works just as well as using the difference vector.

Lastly, for spiral CSF-mobility, denoted as D_{spiral} , we use Equation 6.9:

$$D_{spiral} = \left| \frac{\vec{V}(i, j, k)}{\|\vec{V}(i, j, k)\|} \cdot \frac{\vec{v}_{cross}}{\|\vec{v}_{cross}\|} \right| \quad (6.9)$$

Spiral CSF-mobility is defined as how perpendicular $\vec{V}(i, j, k)$ is to the two former axial and radial CSF-mobility directions. For a more intuitive description, this measure can also be defined as how tangential $\vec{V}(i, j, k)$ is to the circle that is drawn in Figure 6.7.

Now the difference between the left and right side of Figure 6.7 will be addressed. As mentioned before, each datapoint is linked to the closest tangent line point and evaluated accordingly. This means that, for some datapoints, the orientation of \vec{v}_{diff} is not perfectly perpendicular to the orientation of \vec{v}_{tang} . This can be seen on the right-hand side of the figure. If \vec{v}_{diff} was used in this situation to directly compute D_{radial} , a measure that still contains an axial component would be obtained, because it is not perfectly perpendicular to the axial direction. In order to circumvent this, \vec{v}_{diff} was replaced by $\vec{v}_{cross} \times \vec{v}_{tang}$. In doing so, the method can be used for both situations.

All vectors are normalized so that the derived parameters pertain solely to the directionality of the signal and not the CSF-mobility magnitude. All parameters are defined as absolutes because the sign of the measured vector is trivial; CSF-mobility is measured along an axis, but not in the positive or negative direction. For each voxel a check was done to make sure that the following equation holds:

$$D_{axial}^2 + D_{radial}^2 + D_{spiral}^2 = 1 \quad (6.10)$$

Also, each segmented vector field was converted to Paraview (Version 5.11.0) for visualization purposes. Scalar values D_{axial} , D_{radial} and D_{spiral} were colorcoded so enable visual checks. All parameters were derived for all 11 participants in all four ROIs for 12 datasets (one dataset for each of the six cardiac phases and one dataset for each of the six random bins). For the dark tissue ROI, the whole slab was treated as one large vessel cross-section. All values in this ROI are linked to a single tangent line which is oriented perpendicularly to the slab. Apart from that, parameters are computed in the same way as for the three vessel ROIs.

Additional reduction of the MCA ROI

Both the ROI for the basal ganglia and the CSO are assumed to be segmentations without any bifurcations, since no bifurcations can be seen on the b0-image. For the MCA ROI, bifurcations at the medial and lateral part of the ROI can be present. These bifurcations can alter the directionality of the signal in such a way that the results are perturbed: CSF-mobility vectors e_1 might point away from the vessel centerline and thus get a high radial value, while they could be well axially aligned with another centerline running through the bifurcating vessel. For this reason, small sections of the ROI at the distal and lateral part that show bifurcations have been removed. This was done manually for each ROI.

Comparison between cardiac and random binned signal

In order to provide some physiological basis for the directional parameters derived in section 6.1, variations in the directional parameters over the cardiac cycle were tracked and compared to the random binned cycle. A sinusoid was fitted to each cardiac binned and random binned time signal per voxel, where the amplitude and phase of the sinusoid were the fitted parameters. The R^2 was used as a measure for the goodness of fit for the change in signal. The amplitude of the signal was also recorded for analysis. For each voxel of which the goodness of fit was below 0.5, the amplitude was set to zero, as otherwise the amplitudes for bad fits will become unrealistically high. Comparisons between cardiac gated and random signals were assessed for both goodness of fit and signal amplitude.

Statistical analysis

Having done analyses on the CSF-mobility orientation in different ROIs and the pulsatility of all three CSF-mobility parameters, several outcomes can be recognized:

1. average D_{axial} for all 4 ROIs, taken from the cardiac binned dataset.
2. average D_{radial} for all 4 ROIs, taken from the cardiac binned dataset.
3. average D_{spiral} for all 4 ROIs, taken from the cardiac binned dataset.
4. Goodness of Fit for the change in D_{axial} for all 4 ROIs across cardiac and random bins.
5. Goodness of Fit for the change in D_{radial} for all 4 ROIs across cardiac and random bins.
6. Goodness of Fit for the change in D_{spiral} for all 4 ROIs across cardiac and random bins.
7. Signal amplitude for the change in D_{axial} for all 4 ROIs across cardiac and random bins.
8. Signal amplitude for the change in D_{radial} for all 4 ROIs across cardiac and random bins.
9. Signal amplitude for the change in D_{spiral} for all 4 ROIs across cardiac and random bins.

For each subset, a Friedman test was done. For the Friedman test, the null hypothesis is that there are no significant differences between any of the groups in the dataset. If the null hypothesis is rejected (at $p < 0.05$), meaning that there was at least one group significantly different from another group within the subset, a Wilcoxon signed-rank test was applied to that dataset as well. This signed-rank test will compare each group with the other groups within the dataset to determine which are significantly different from each other. This means that for points 1, 2 and 3 on the list, the signed-rank test will be done six times for each point in order to find the p-value for differences between the ROIs. For points 4-9, signed-rank tests will be done between each cardiac and random binned ROI, so within each ROI, to assess whether we see any significant difference in pulsatility and amplitude when comparing both binning strategies (that means four signed-rank tests per parameter). Lastly, to see whether there are any variations in pulsatility and amplitude between ROIs, differences between the cardiac datasets of each ROI will also be assessed, providing six more signed-rank tests.

6.2 Results

The three parameters derived in section 6.1 will now be presented for all four ROIs. Results will be assessed qualitatively using images of the 3D vector field segmentations from Paraview and quantitatively as well.

6.2.1 Qualitative assessment shows occurrence of homogeneous regions within the SAS

The 3D representations of each ROI were used to check whether the directional CSF-mobility parameter values (values for D_{axial} , D_{radial} and D_{spiral}) of each vector corresponded to their orientation with respect to the centerline. These 3D representations for the larger anatomy, the SAS around the MCA, can be seen Figure 6.8. The colorcodings demonstrate the axial, radial and spiral distribution of the CSF-mobility vectors along the vessel. Most vectors are aligned to the centerline, hence the high axial values in the figure. This is the case for most vectors, but some express a radial or spiral preference. At first, it might seem like the radial and spiral parameters are just the opposite of the axial parameter. However, this is not the case. The differences between radial and spiral can be seen in Figure 6.9. Note how the encircled vectors closest to the chosen viewpoint, pointing outward from the vessel are assigned high radial values, while vectors that circle around the centerline, are assigned high spiral values. Because of Equation 6.10, vectors that demonstrate low values for both images are oriented along the vessel centerline and thus have a high axial value. In Figure 6.8, large regions containing homogeneously high values for axial and spiral CSF-mobility can be seen. Subfigure C shows the occurrence of high spiral values in the right part of the ROI, where the yellow lines tend to cross over from the top part of the vessel to the lower part (encompassed with a circle). This phenomenon shows up in multiple participants, of which two are compared in Figure 6.10. The occurrence of homogeneous regions with high axial or spiral values is in accordance with the expected axes of freedom that a hollow cylinder constitutes (freedom to move along the vessel and around, e.g. in the axial and spiral direction).

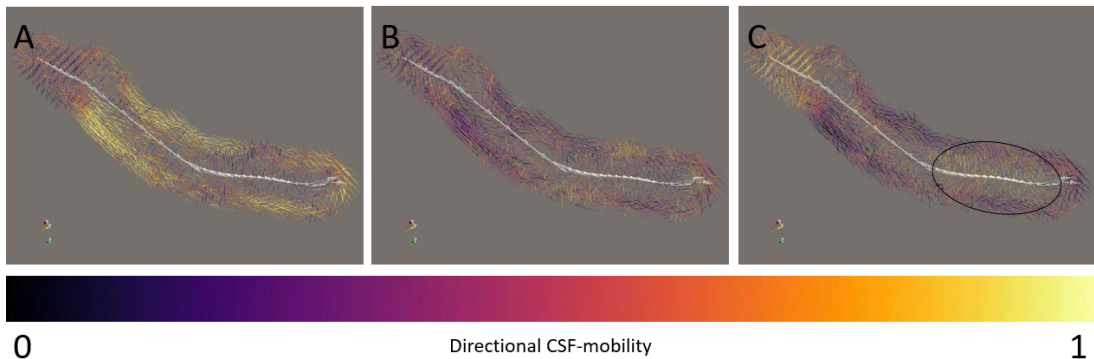


Figure 6.8: Colorcoded 3D representations of the $e_1\lambda_1$ vector field of the SAS around the MCA. A is colorcoded according to the axial CSF-mobility, B is colorcoded according to the radial CSF-mobility and C is colorcoded according to the spiral CSF-mobility.

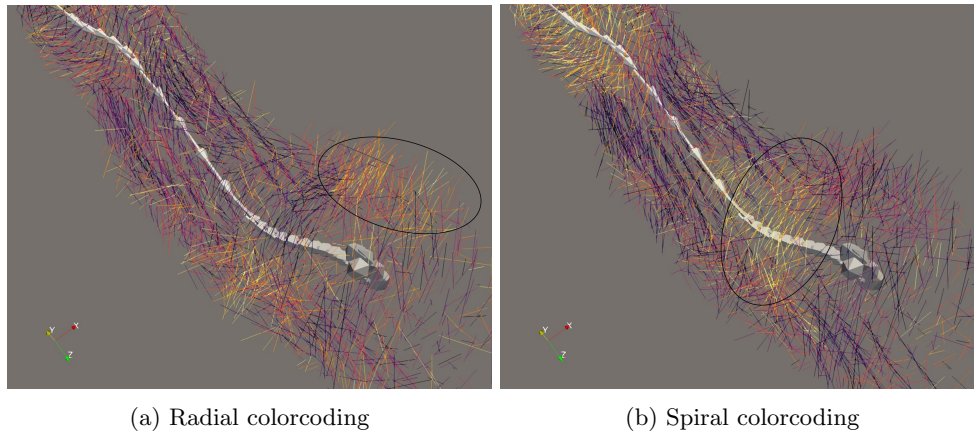


Figure 6.9: Comparison between radial and spiral CSF-mobility orientations in an MCA ROI

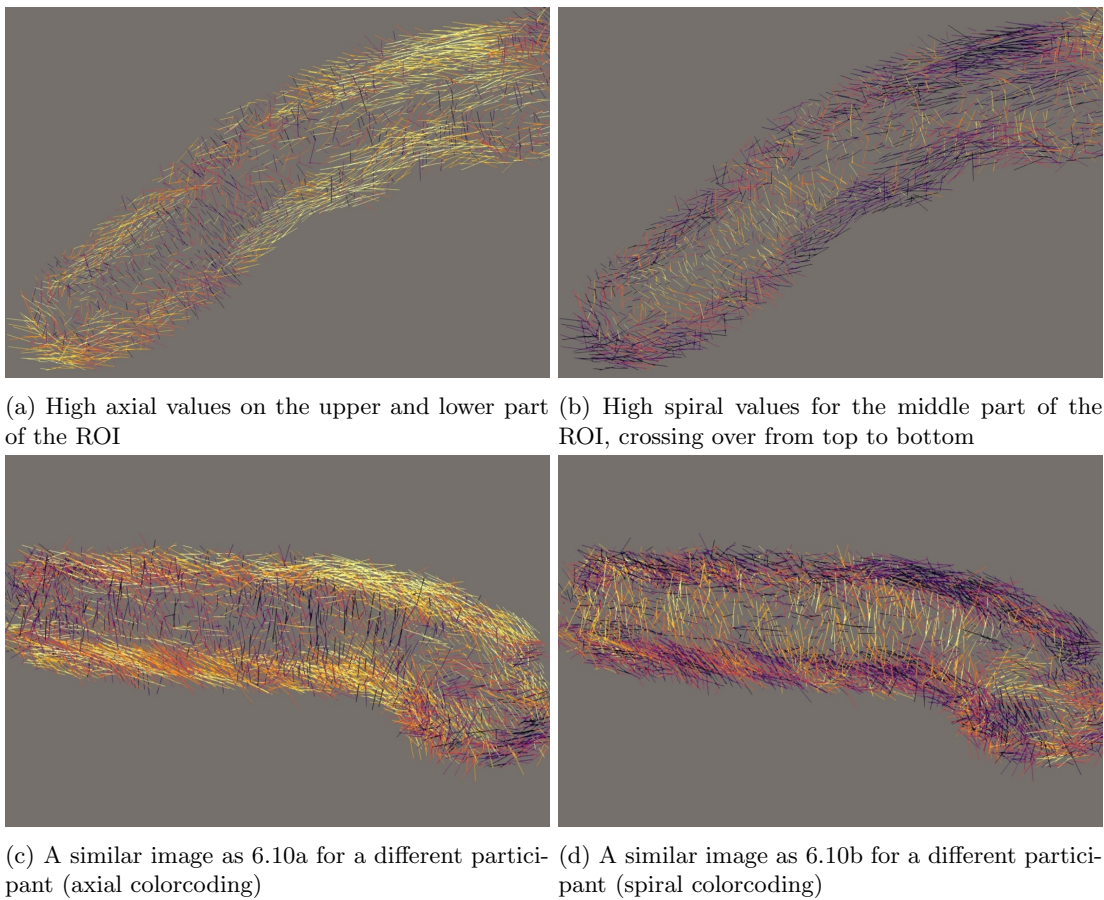


Figure 6.10: Illustration of homogeneous regions occurring similarly in multiple participants (centerline is removed for clarity).

6.2.2 Qualitative assessment of the PVS shows ambiguous results

The 3D representations of the basal ganglia and CSO ROI of one of the participants can be seen in Figures 6.11a and 6.11b. The orientations in the PVS seem more random than in the SAS. However, both PVS ROIs describe similar trends in orientation, with some regions showing systematically low axial values. This can be seen in Figure 6.11b, where a multitude of lines from PVS in the CSO seem oriented perpendicularly to the centerline. A similar trend can be seen in PVS in the basal ganglia from

another participant in Figure 6.12. When looking at the radial and spiral values for those regions, there does not seem to be a clear preference for either. This could make quantitative assessment a challenge.

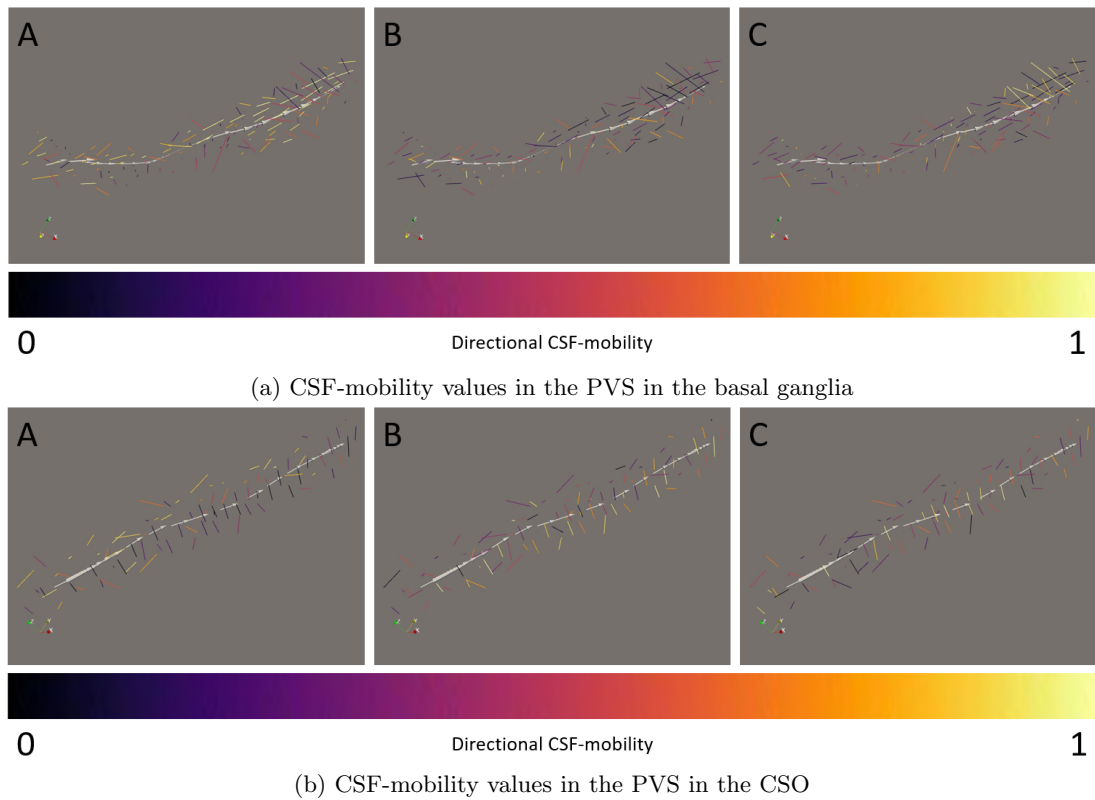


Figure 6.11: Colorcoded 3D representations of the $e_1\lambda_1$ vector field of the PVS in the basal ganglia (6.11a) and around a penetrating vessel in the CSO (6.11b). A describes axial CSF-mobility, B describes radial CSF-mobility and C describes spiral CSF-mobility.

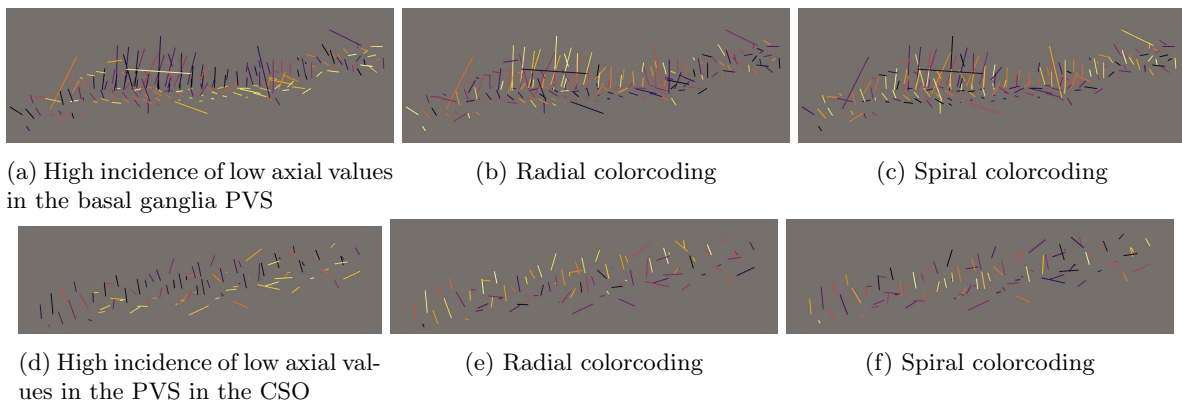


Figure 6.12: Illustration of regions with low axial values and how those seem to be divided into high radial and high spiral values (centerline is removed for clarity).

6.2.3 Quantitative assessment of directional CSF-mobility per ROI

Average CSF-mobility values or each parameter have been derived for each participant, each ROI and each cardiac phase, cardiac and random. Differences between ROIs for the different parameters are shown in Figure 6.9 and Table 6.1. The p-values for the signed-rank test for each of the parameters are given in Table 6.2. The Friedman test was significant for all three subsets ($p < 0.01$), meaning that, for all three subsets, at least one group is significantly different from another.

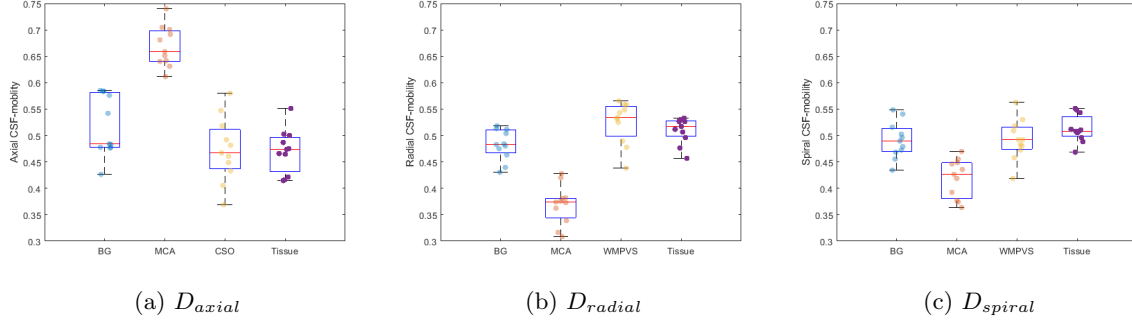


Figure 6.13: Directional mobility differences between ROIs

The differences between the MCA and the other ROIs are quite clear. The largest difference is in parameter D_{axial} : For the MCA, the average D_{axial} is 0.6684, while for the closest other ROI, D_{axial} is 0.5179. Note that Equation 6.10 still holds for these parameters: a high average axial value will almost always lower the average radial and spiral values of an ROI. Significant differences between groups were found when comparing the SAS ROI to all others for all parameters ($p < 0.001$ for all values). Furthermore, measurements in the basal ganglia ROI are significantly different from the dark tissue ROI for all parameters.

	Basal Ganglia	MCA	CSO	Tissue
Axial	0.5179 +/- 0.0625	0.6684 +/- 0.0421	0.4731 +/- 0.0677	0.4703 +/- 0.0453
Radial	0.4822 +/- 0.032	0.3690 +/- 0.0404	0.5246 +/- 0.0439	0.5099 +/- 0.0267
Spiral	0.4913 +/- 0.0379	0.4189 +/- 0.0400	0.4925 +/- 0.0418	0.5128 +/- 0.0282

Table 6.1: Average CSF-mobility values (CI=95%) for each ROI.

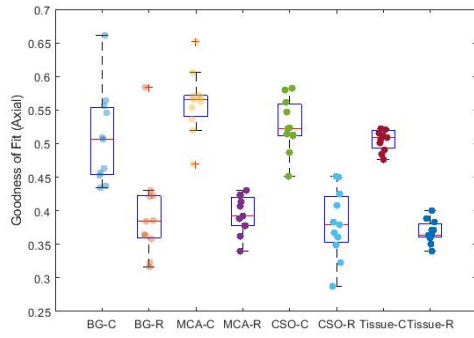
<i>Axial</i>	Basal Ganglia	MCA	CSO	Tissue
Basal Ganglia		<0.001	0.1016	0.0420
MCA	<0.001		<0.001	<0.001
CSO	0.1016	<0.001		1
Tissue	0.0420	<0.001	1	
<i>Radial</i>	Basal Ganglia	MCA	CSO	Tissue
Basal Ganglia		<0.001	0.0186	0.0322
MCA	<0.001		<0.001	<0.01
CSO	0.0186	<0.001		0.3652
Tissue	0.0322	<0.001	0.3652	
<i>Spiral</i>	Basal Ganglia	MCA	CSO	Tissue
Basal Ganglia		<0.001	0.5195	0.0137
MCA	<0.001		<0.001	<0.001
CSO	0.5195	<0.001		0.2061
Tissue	0.0137	<0.001	0.2061	

Table 6.2: P-values for the signed-rank test for all D_{axial} , D_{radial} and D_{spiral}

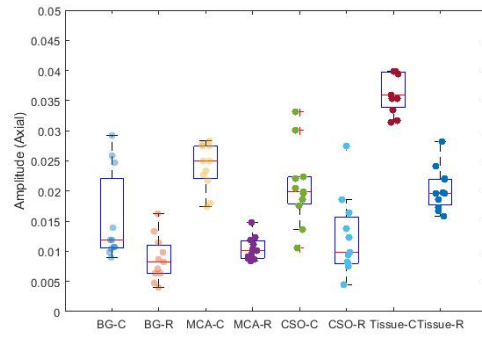
6.2.4 Comparison between cardiac and random binned signal

On the left side of Figure 6.14, the differences in goodness of fit for the sinusoids fitted on the cardiac and random binned signals for all ROIs as described in section 6.1 are illustrated. In Figure 6.14, the goodness of fit of all cardiac binned groups is systematically at least 0.1 higher than their random binned counter parts (see also Table 6.3). These findings are also demonstrated by the p-values for the signed-rank test in Table 6.4. In this table, the p-values for comparison between cardiac and random binned signal are given and they all indicate a significant difference ($p < 0.05$). In Table 6.5, the p-values for differences between the cardiac goodness of fit for each ROI can be seen. In this table, the

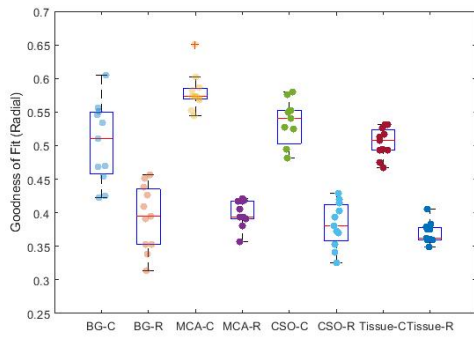
most notable finding is that the p-value for difference between the MCA and tissue ROI is significant, ($p < 0.003$ for all three parameters), while comparisons between tissue, basal ganglia and CSO are all insignificant. Since variations in either axial, radial or spiral values all constitute a change in orientation, all subfigures from the left column from Figure 6.14 look similar. This similarity indicates that orientation changes typically occur over multiple axes, because otherwise one boxplot would have looked different from the others. The boxplots for amplitude differences between ROIs are seen on the right side. Just as with the goodness of fit values, the amplitudes of the cardiac binned group are systematically higher than their random binned counterparts. Note that, as described in Section 6.1, voxels with a low goodness of fit (< 0.5) have had their amplitude set to 0. This means that ROIs that have a worse fit, on average, will get a lower amplitude. This should be kept in mind when assessing the differences in amplitudes. P-values of those differences are shown in Table 6.8 and show that all differences between cardiac and random binned are significant ($p < 0.05$), but this should be approached with some scepticism because ROIs with a worse fit, meaning the random binned ROIs, have their amplitude values set to zero more often than the cardiac binned ROIs. Table 6.6 describes the average values for the amplitude of the fit. In this table, it is indicated that the tissue ROI has the highest amplitudes, then the MCA, then the CSO and then the basal ganglia ((0.0383 + / - 0.0096), (0.0240 + / - 0.0042), (0.0207 + / - 0.0070) and (0.0153 + / - 0.0081) for the axial cardiac values, respectively). Lastly, Table 6.7 provides p-statistics for the signed-rank test between ROIs for the cardiac binned signal amplitude.



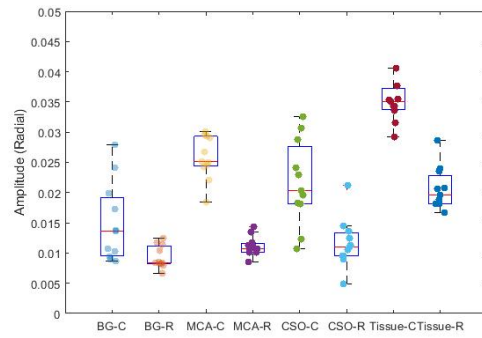
(a) Goodness of fit for axial CSF-mobility



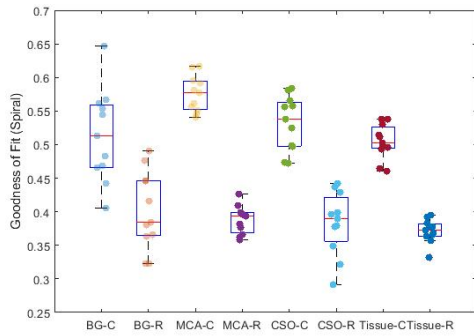
(b) Amplitude for fit for axial CSF-mobility



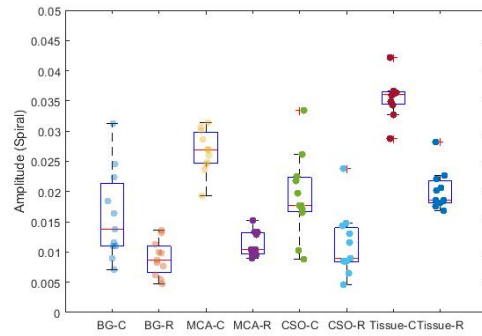
(c) Goodness of fit for radial CSF-mobility



(d) Amplitude for fit for radial CSF-mobility



(e) Goodness of fit for spiral CSF-mobility



(f) Amplitude for fit for spiral CSF-mobility

Figure 6.14: Averages for voxel-wise sinusoidal fits for each ROI for each parameter (axial, radial and spiral).

	Basal Ganglia (C)	MCA (C)	CSO (C)	Tissue (C)
Axial	0.5082+/-0.0764	0.5616+/-0.0507	0.5268+/-0.0431	0.5055+/-0.0172
Radial	0.5037+/-0.0653	0.5799+/-0.0309	0.5022+/-0.1342	0.5044+/-0.0237
Spiral	0.5136+/-0.0755	0.5757+/-0.0293	0.5317+/-0.0447	0.5042+/-0.0286
	Basal Ganglia (R)	MCA (R)	CSO (R)	Tissue (R)
Axial	0.3959+/-0.0800	0.3941+/-0.0309	0.3805+/-0.0559	0.3687+/-0.0187
Radial	0.3934+/-0.0528	0.3987+/-0.0216	0.3823+/-0.0365	0.3698+/-0.0170
Spiral	0.4018+/-0.0635	0.3880+/-0.0231	0.3830+/-0.0518	0.3713+/-0.0194

Table 6.3: Average goodness of fit for each parameter for each ROI (n=11) (CI=95%). (C): Cardiac binned data. (R): Random binned data.

	Basal Ganglia	MCA	CSO	Tissue
Axial	0.0186	<0.001	<0.001	<0.001
Radial	<0.001	<0.001	<0.001	<0.001
Spiral	0.0137	<0.001	<0.001	<0.001

Table 6.4: Signed-rank test for goodness of fit for the sinusoid fitted to the CSF-mobility signal. Each value signifies the p-value for the difference between the cardiac and random gated signal for each ROI and for each parameter (n=11).

<i>Axial</i>	Basal Ganglia	MCA	CSO	Tissue
Basal Ganglia		0.0674	0.3652	0.8984
MCA	0.0674		0.1748	0.0029
CSO	0.3652	0.1748		0.2402
Tissue	0.8984	0.0029	0.2402	
<i>Radial</i>	Basal Ganglia	MCA	CSO	Tissue
Basal Ganglia		0.0049	0.7646	0.8311
MCA	0.0049		0.0137	<0.001
CSO	0.7646	0.0137		0.2061
Tissue	0.8311	<0.001	0.2061	
<i>Spiral</i>	Basal Ganglia	MCA	CSO	Tissue
Basal Ganglia		0.0244	0.3203	0.7646
MCA	0.0244		0.0244	<0.001
CSO	0.3203	0.0244		0.1016
Tissue	0.7646	<0.001	0.1016	

Table 6.5: P-values for the signed rank test between each cardiac ROI for goodness of fit for each parameter (n=11).

	Basal Ganglia (C)	MCA (C)	CSO (C)	Tissue (C)
Axial	0.0153+/- 0.0081	0.0240+/-0.0042	0.0207+/-0.0070	0.0383+/-0.0096
Radial	0.0150+/-0.0072	0.0259+/-0.0040	0.0217+/-0.0077	0.0371+/-0.0091
Spiral	0.0160+/-0.0082	0.0267+/-0.0039	0.0193+/-0.0075	0.0379+/-0.0096
	Basal Ganglia (R)	MCA (R)	CSO (R)	Tissue (R)
Axial	0.0088+/-0.0041	0.0105+/-0.0021	0.0124+/-0.0071	0.0203+/-0.0039
Radial	0.0093+/-0.0020	0.0111+/-0.0018	0.0116+/-0.0045	0.0206+/-0.0038
Spiral	0.0090+/-0.0032	0.0112+/-0.0023	0.0112+/-0.0058	0.0202+/-0.0035

Table 6.6: Average Amplitudes for each parameter for each ROI (n=11) (CI=95%). (C): Cardiac binned data. (R): Random binned data (n=11).

	Basal Ganglia	MCA	CSO	Tissue
Axial	0.0137	<0.001	<0.001	<0.001
Radial	0.0186	<0.001	<0.001	<0.001
Spiral	0.0186	<0.001	0.0020	<0.001

Table 6.7: Signed-rank test for amplitude for the sinusoid fitted to the CSF-mobility signal. Each value signifies the p-value for the difference between the cardiac and random gated signal for each ROI and for each parameter (n=11).

<i>Axial</i>	Basal Ganglia	MCA	CSO	Tissue
Basal Ganglia		0.0098	0.0244	<0.001
MCA	0.0098		0.2061	<0.001
CSO	0.0244	0.2061		<0.001
Tissue	<0.001	<0.001	<0.001	
<i>Radial</i>	Basal Ganglia	MCA	CSO	Tissue
Basal Ganglia		<0.001	0.0322	<0.001
MCA	<0.001		0.1748	0.0020
CSO	0.0322	0.1748		<0.001
Tissue	<0.001	0.0020	<0.001	
<i>Spiral</i>	Basal Ganglia	MCA	CSO	Tissue
Basal Ganglia		<0.001	0.1748	<0.001
MCA	<0.001		0.0137	<0.001
CSO	0.1748	0.0137		<0.001
Tissue	<0.001	<0.001	<0.001	

Table 6.8: P-values for the signed rank test between each cardiac ROI for amplitude for each parameter (n=11).

6.3 Discussion

This study provided an assessment of the e_1 orientation of CSF-mobility with respect to vessel orientation. Large homogeneous regions with similarly high values for axial and spiral CSF-mobility are easily recognizable in the SAS ROI. This is congruent with the axes of freedom for the geometry of a hollow cylinder (space to move around in a longitudinal, but also in a swirling fashion). For PVS around the smaller cerebral vessels, it is more difficult to see any trends. Some sections of PVS indicate a high incidence of low axial values, but this is not as prevalent in quantitative measurements. Quantitatively, there is a clear preference for axial orientation in the SAS and p-statistics for the directional differences between the basal ganglia ROI and the dark tissue ROI are also significant. Sinusoidal fits for all three parameters over all ROIs indicate a change in orientation that is congruent with the cardiac rhythm. Amplitudes for each sinusoidal fit over the cardiac binned signal also indicate variations that seem to correlate with vessel size since the largest vessel ROI also has the highest amplitudes. The fact that a significant increase in goodness of fit for cardiac binning compared to random binning has been observed demonstrates the influence of cardiac pulsations on the directionality of fluid dynamics in the CSF. Sinusoidal fits for the darker tissues also indicate that the pulsatility of the signal persists in regions with relative low signal-to-noise ratio (SNR) and hint at a possibly stronger influence of noise on the amplitude of the fit. A more in-depth analysis of the aforementioned findings and others will now follow.

6.3.1 Directional CSF-mobility differences between ROIs

There is a clear high incidence of axially oriented CSF-mobility in the SAS around the MCA. This is significantly different from the tissue ROI (0.4703 ± 0.0453) and the other smaller vessel ROIs (0.5179 ± 0.0625 for the basal ganglia, 0.4731 ± 0.0677 for the CSO) as shown in Figure 6.13 and Table 6.1. The axial preference is in accordance with the findings from Harrison et al. in a study where the loss of signal within the MCA was measured under the influence of different MPG's (see Figure 6.15) [14]. Their findings namely indicate that the CSF-mobility orientations in the MCA are roughly aligned with the vessel orientation, so their dataset would constitute similar high axial values.

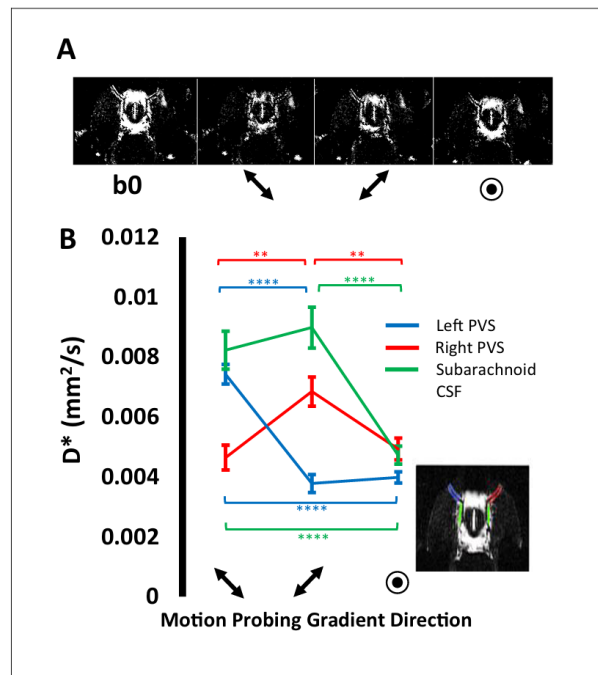


Figure 6.15: A DTI experiment in SAS in a rat brain. **A:** The signal loss for three orthogonal MPG's compared to the b0-image (the rightmost MPG is through-plane). **B:** Signal loss when comparing MPG's perpendicular and parallel to the vessel orientation [14].

The fact that we do not see such a high incidence of axial CSF-mobility in the smaller PVS could be explained by several causes. What is clear from Figure 6.13 and Table 6.1 is that the smaller PVS have much more similarities with the CSF-mobility profile of the tissue ROI than with the profile of the SAS. Since the basal ganglia and CSO ROIs have more voxels bordering darker regions, it could be that these border voxels include more noisy signal and thus constitute a more noisy result compared to the MCA ROI (at least, the amount of CSF-signal in the PVS is lower than in the SAS around the MCA). A way to check for this would be to erode the CSF-mask for the MCA from the inside out to get a mask that includes only border voxels and compare with previous results, or to check the relation between greyscale values and each mobility parameter. Another reason for the noise-like behavior in the smaller vessel ROIs could be that the displacement velocities are out of range for the chosen b-value. If that were the case and assuming that the displacement velocities are too low (more in the diffusion-like range), it would reinforce the theory on PVS dynamics as explained in the mixing model: flow in the SAS and mixing in the PVS. Assuming that mean displacement in the PVS is lower than in the SAS, a new scan with higher b-values could provide more insight.

6.3.2 Relating the motion-sensitizing gradient strength sensitivity to directional CSF-mobility

The measured values for each CSF-mobility parameter are dependent on the range of speeds for which the MRI sequence is sensitive. Gathering information on the range of displacement speeds in the SAS and PVS could prove useful for this: If we measure low axial values, is this because there is not much displacement in that direction, or because the displacement is outside of the sensitivity range? When looking at the literature for physiological phenomena that might cause motion in the PVS, we can recognize cardiac pulsatility through the vessel as a cause for radial displacement, influencing fluid dynamics in the perivascular space [27]. In our case, the chosen motion-sensitizing gradient is sensitive to displacement speeds around 5 mm/s . Assessment of the derivative of the radius change of cerebral vessels throughout the cardiac cycle could provide the information needed to identify the range of radial displacement speeds and relate that to the V_{enc} that was used. In a different article, Asgari et al. have created a model of flow speeds in the arterial PVS where they measure peak velocities of $276\ \mu\text{m/s}$ [7]. If the velocities in this model are similar to the real velocities in the arterial PVS, the applied motion-sensitizing gradient would be too high to measure displacement in the PVS, which could explain why there is no clear preferential direction for the PVS ROIs.

6.3.3 Reliability of D_{axial} , D_{radial} and D_{spiral}

The spiral values for each ROI were the least conclusive. The p-values in Table 6.2 report some significance, but these should be approached with some scepticism. This is because of the following limitation: Spiral and radial values are highly influenced by their *position* relative to the centerline, while axial values are mostly influenced by their *orientation* relative to the centerline. In larger CSF-filled spaces such as the SAS, this is not an issue because we have large vessel diameters and voxels close to the centerline are not included in the mask as these are voxels only containing blood. However, in PVS, where the vessel diameter is often just one voxel, the differentiation between radial and spiral values is not as distinct and small deviations in the centerline positioning can have implications for the radial-spiral relation of a vessel. Small deviations in the centerline positioning can occur due to strong curves in the ROI. An example of how the distance between the centerline and the vector point influences this can be seen in Figure 6.16. Scans with a higher resolution or zero-filling of the k-space could have a positive influence on the centerline fitting and thus make differentiation between radial and spiral values more reliable. Otherwise, combining both radial and spiral values to a single metric that measures how perpendicular each vector is to the centerline could also circumvent this issue.

6.3.4 Differences in qualitative and quantitative assessment

The incidence of large regions with similar values for one of the parameters is evident in some examples of the SAS and the PVS (as shown in Figures 6.10 and 6.12). However, such incidence is not reflected in the quantitative analyses, meaning that figures such as Figure 6.13 do not convey any of this behavior. This might be explained by the fact that the reported quantitative values are averaged over a large ROI that contains different orientations along the vessel. Although visual checks on the vector field as

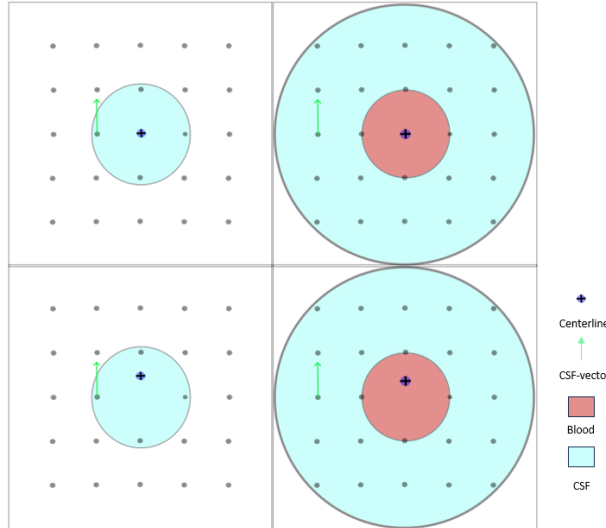


Figure 6.16: Illustration of different centerline positions. The centerline is going through-plane. Left side illustrates the situation for PVS. On this side, a shift in the centerline positioning will cause a large change in D_{radial} and D_{spiral} . On the right side, which illustrates this situation for the SAS, the shift in centerline positioning will cause a smaller change in D_{radial} and D_{spiral} .

portrayed in Paraview already reflect a clear pattern with large, homogeneous, axial and spiral regions, it might be interesting to attempt to visualize this quantitatively as well. For this reason, it could be interesting to combine the CSF-mobility parameters D_{axial} , D_{radial} and D_{spiral} with other readily available scalar values from the CSF-STREAM dataset. Comparing the incidence of high values in one of the three directions with scalar values like FA, MD and eigenvalues and vectors could provide a better understanding for how these patterns come about.

6.3.5 Amplitude of CSF-mobility orientation change with cardiac and random cycle across ROIs

The most prominent finding in the amplitude values of D_{axial} , D_{radial} and D_{spiral} for each ROI is that the amplitudes for the noise ROI are significantly higher than other ROIs. Explanations for this high amplitude could be explained by the influence of noise in this ROI. As the amount of signal in the b_0 -image decreases, the reliability of the e_1 orientation also decreases [16]. This could make a signal less stable and thus exhibit larger e_1 angle changes, especially since the current analysis was done on normalized vectors. DTI research on skeletal muscle has also indicated that reliability of e_1 is influenced weakly by FA and strongly by $\lambda_2 \cdot \lambda_3$ relation [28]. Moreover, low SNR in combination with variations in T_2 can have strong implications for FA and λ_3 values for T_2 -weighted scans [29]. Further research on the variations in T_2 for darker tissue could provide some insight into the reliability of e_1 orientation under the influence of $\lambda_2 \cdot \lambda_3$ relation. Influence of FA on the signal could also be assessed in a rather simple manner. For instance, voxels that have a more isotropic profile typically have eigenvalues that are close to each other. Since the eigenvalues correspond to the eigenvectors, which are all oriented perpendicularly to each other, small changes in λ_1 , λ_2 and λ_3 could change the hierarchy and thus flip the orientation of the e_1 vector with 90 degrees. Voxel-wise assessment of relatively large orientational changes, cross-referencing with the FA of that same voxel, could provide insight into the influence of FA for the amplitude of changes in orientation.

When comparing the amplitudes of PVS and SAS, we can see a significantly higher amplitude in the SAS, which is in accordance with findings from Hirschler et al. [24]. They reported a larger amplitude in the sinusoidal fit for CSF-mobility, which is more closely related to variations in eigenvalues than eigenvectors. Combining findings from this study and ours, one could argue that there is a correlation between the magnitudes of CSF-mobility (λ) and the directional variations (e_1).

This study assesses amplitude changes in the context of orientation. The orientational amplitudes that have been measured do not rise above 0.05. Since each of the measures is a dot-product between

two vectors, the maximum difference in orientation between the two vectors is 90 degrees. When considering the most exaggerated version of this signal, we could have an e_1 vector that changes from 1 to 0 over the whole cardiac cycle. This would mean a difference between the minimum and maximum of 90 degrees and thus an amplitude of 45 degrees (assuming that the average is oriented at 45 degrees from the tangent orientation as well). Multiplying this with a rough estimate of the maximum in measured amplitudes, we get $0.05 * 45 = 2.25$ degrees change. This indicates how small the orientational changes we measure are. It could be interesting to combine these changes with changes in λ_1 i.e. analyze the unnormalized vectors.

6.3.6 Limitations

This study has assessed the directionality of the CSF-mobility with respect to vessel orientation. This means that no inferences can be made on the magnitudes of CSF-mobility. Also, no assessment of the influence of noise (ROI outside of the brain) has been done, meaning that here is no information on SNR and its influence on variations in orientation. Lastly, the chosen b-value for this sequence is chosen as an aggregate so that the sequence can measure signal attenuation due to dephasing in the SAS as well as the PVS. This makes it so that the CSF-mobility measurements in both regions are more reliable, but the b-value itself might not be ideal for the dynamic properties of the PVS.

Chapter 7

Conclusion

Directionality assessment of CSF-mobility in the PVS is proven to be a topic of interest for the field of CSF-mediated brain clearance. Comparison of the CSF-mobility orientation to vessel orientation and decomposition into axial, radial and spiral values has proven to be useful for qualitative analysis, mostly in the SAS, where one can discern a clear pattern of the fluid dynamics in multiple participants. Quantitative analysis indicates similarities between PVS ROIs that require further research into the the influence of signal strength, resolution and the b-value. Besides these possible confounding factors, dissimilarities measured between SAS and PVS can contribute to the discussion on perivascular fluid dynamics, and the variations of the measured signal over the cardiac phase indicate a physiological basis for the provided framework. The significant differences measured between cardiac and random binned signal provide strong evidence for the role of cardiac pulsations as a driving force for brain clearance. Further research is required for more profound conclusions. The combination of D_{axial} , D_{radial} and D_{spiral} with scalar values such as FA, MD, λ_1 , but also secondary and tertiary eigenvalues and vectors could provide more insight.

Bibliography

- [1] ZiMian Wang et al. “Evaluation of specific metabolic rates of major organs and tissues: comparison between nonobese and obese women”. In: *Obesity* 20.1 (2012), pp. 95–100.
- [2] Shan Liao and Timothy P Padera. “Lymphatic function and immune regulation in health and disease”. In: *Lymphatic research and biology* 11.3 (2013), pp. 136–143.
- [3] Joel Ramirez et al. “Imaging the perivascular space as a potential biomarker of neurovascular and neurodegenerative diseases”. In: *Cellular and molecular neurobiology* 36 (2016), pp. 289–299.
- [4] Stephen B Hladky and Margery A Barrand. “Mechanisms of fluid movement into, through and out of the brain: evaluation of the evidence”. In: *Fluids and Barriers of the CNS* 11 (2014), pp. 1–32.
- [5] Jeffrey J Iliff et al. “A paravascular pathway facilitates CSF flow through the brain parenchyma and the clearance of interstitial solutes, including amyloid β ”. In: *Science translational medicine* 4.147 (2012).
- [6] RO Carare et al. “Solutes, but not cells, drain from the brain parenchyma along basement membranes of capillaries and arteries: significance for cerebral amyloid angiopathy and neuroimmunology”. In: *Neuropathology and applied neurobiology* 34.2 (2008), pp. 131–144.
- [7] Mahdi Asgari, Diane De Zélicourt, and Vartan Kurtcuoglu. “Glymphatic solute transport does not require bulk flow”. In: *Scientific reports* 6.1 (2016).
- [8] Lucy Zhao et al. “Physiology of glymphatic solute transport and waste clearance from the brain”. In: *Physiology* 37.6 (2022), pp. 349–362.
- [9] Stephen B Hladky and Margery A Barrand. “The glymphatic hypothesis: the theory and the evidence”. In: *Fluids and Barriers of the CNS* 19.1 (2022), pp. 1–33.
- [10] Lori A Ray and Jeffrey J Heys. “Fluid flow and mass transport in brain tissue”. In: *Fluids* 4.4 (2019), p. 196.
- [11] John H Thomas. “Fluid dynamics of cerebrospinal fluid flow in perivascular spaces”. In: *Journal of the Royal Society Interface* 16.159 (2019), p. 20190572.
- [12] Humberto Mestre et al. “Flow of cerebrospinal fluid is driven by arterial pulsations and is reduced in hypertension”. In: *Nature communications* 9.1 (2018), p. 4878.
- [13] Jeffrey J Iliff et al. “Brain-wide pathway for waste clearance captured by contrast-enhanced MRI”. In: *The Journal of clinical investigation* 123.3 (2013), pp. 1299–1309.
- [14] Ian F Harrison et al. “Non-invasive imaging of CSF-mediated brain clearance pathways via assessment of perivascular fluid movement with diffusion tensor MRI”. In: *Elife* 7 (2018), e34028.
- [15] Lydiane Hirschler et al. “High resolution T2-prepared MRI enables non-invasive assessment of CSF flow in perivascular spaces of the human brain”. In: *Proceedings of the 27th Annual Meeting of ISMRM, Montreal, QC, Canada*. 2019.
- [16] Jonathan AD Farrell et al. “Effects of SNR on the accuracy and reproducibility of DTI-derived fractional anisotropy, mean diffusivity, and principal eigenvector measurements at 1.5 T”. In: *Journal of magnetic resonance imaging: JMRI* 26.3 (2007), p. 756.
- [17] Robert W Brown et al. *Magnetic resonance imaging: physical principles and sequence design*. John Wiley & Sons, 2014.
- [18] Lisa C Krishnamurthy et al. “Dependence of blood T2 on oxygenation at 7 T: in vitro calibration and in vivo application”. In: *Magnetic resonance in medicine* 71.6 (2014), pp. 2035–2042.

- [19] Jolanda M Spijkerman et al. “T2 mapping of cerebrospinal fluid: 3T versus 7T”. In: *Magnetic Resonance Materials in Physics, Biology and Medicine* 31 (2018), pp. 415–424.
- [20] Elizabeth M Charles-Edwards and M deSouza Nandita. “Diffusion-weighted magnetic resonance imaging and its application to cancer”. In: *Cancer imaging* 6.1 (2006), p. 135.
- [21] Martijn Froeling et al. “Diffusion tensor MRI of the heart—in vivo imaging of myocardial fiber architecture”. In: *Current Cardiovascular Imaging Reports* 7 (2014), pp. 1–11.
- [22] Yoshitaka Bito et al. “Low b-value diffusion tensor imaging for measuring pseudorandom flow of cerebrospinal fluid”. In: *Magnetic Resonance in Medicine* 86.3 (2021), pp. 1369–1382.
- [23] DD Stark, WG Bradley, and WG Bradley. “Magnetic Resonance Imaging vol. 3”. In: *St. Louis, MO, Mosby* (1999).
- [24] Lydiane Hirschler. “Effects of the cardiac and respiratory cycles on CSF-mobility in human subarachnoid and perivascular spaces”. In: *Proceedings of the 31st Annual Meeting of ISMRM, London, UK*. 2022.
- [25] Qiuting Wen et al. “Assessing pulsatile waveforms of paravascular cerebrospinal fluid dynamics using dynamic diffusion-weighted imaging (dDWI)”. In: *NeuroImage* 260 (2022), p. 119464.
- [26] *Image of brain cross-section*. https://www.stepwards.com/?page_id=3067. Accessed: 2023-15-05.
- [27] Julian Rey and Malisa Sarntinoranont. “Pulsatile flow drivers in brain parenchyma and perivascular spaces: a resistance network model study”. In: *Fluids and Barriers of the CNS* 15.1 (2018), pp. 1–11.
- [28] Conrad Rockel and Michael D Noseworthy. “An exploration of diffusion tensor eigenvector variability within human calf muscles”. In: *Journal of magnetic resonance imaging* 43.1 (2016), pp. 190–202.
- [29] Martijn Froeling et al. “DTI of human skeletal muscle: the effects of diffusion encoding parameters, signal-to-noise ratio and T2 on tensor indices and fiber tracts”. In: *NMR in Biomedicine* 26.11 (2013), pp. 1339–1352.